Humoral regulation of iron metabolism by extracellular vesicles drives antibacterial response

Huijuan Kuang[1,6], Geng Dou[1,6], Linfeng Cheng[2], Xiangdong Wang[1], Haokun Xu[1], Xuemei Liu[1,3], Feng Ding[1], Xiaoshan Yang[4], Siying Liu[1], Lili Bao[1], Huan Liu[5], Yao Liu[3], Bei Li[1], Yan Jin [1] ✉ & Shiyu Liu [1] ✉

Immediate restriction of iron initiated by the host is a critical process to protect against bacterial infections and has been described in the liver and spleen, but it remains unclear whether this response also entails a humoral mechanism that would enable systemic sequestering of iron upon infection. Here we show that upon bacterial invasion, host macrophages immediately release extracellular vesicles (EVs) that capture circulating iron-containing proteins. Mechanistically, in a sepsis model in female mice, *Salmonella enterica* subsp. *enterica* serovar Typhimurium induces endoplasmic reticulum stress in macrophages and activates inositol-requiring enzyme 1α signaling, triggering lysosomal dysfunction and thereby promoting the release of EVs, which bear multiple receptors required for iron uptake. By binding to circulating iron-containing proteins, these EVs prevent bacteria from iron acquisition, which inhibits their growth and ultimately protects against infection and related tissue damage. Our findings reveal a humoral mechanism that can promptly regulate systemic iron metabolism during bacterial infection.

Bacterial infection can lead to bacteremia or even sepsis, threatening human life in serious cases[1]. As iron participates in critical biological processes, including nucleic acid synthesis, electron transport and redox reactions[2] in both host and bacterial pathogens, the host immediately restricts the availability of iron after bacterial invasion and thereby limits the infection, which is termed nutritional immunity[2]. It has been well proven that liver- and spleen-resident macrophages take up iron-containing proteins via membrane receptors, including transferrin receptor (TfR), LDL-related protein 1 (CD91) and hemoglobin-haptoglobin receptor (CD163), which bind transferrin-bound iron, heme-hemopexin and hemoglobin-haptoglobin, respectively, to recycle and sequester iron and thus starve bacteria[3,4]. These studies focus on cell-dependent regulation of iron metabolism. Given that the iron-containing proteins existing in body fluid may be distant from tissue-resident macrophages and can be acquired by the invading bacteria[2], it is reasonable to hypothesize that the host had evolved undiscovered humoral regulation mechanisms to promptly acquire and recycle the circulating iron for rapid iron sequestration.

EVs are released by cells into multiple body fluids[5,6] but the role of EVs in infection is largely unknown. Notably, emerging evidence indicates that EV release during infection may be associated with iron

[1]State Key Laboratory of Military Stomatology & National Clinical Research Center for Oral Diseases & Shaanxi International Joint Research Center for Oral Diseases, Center for Tissue Engineering, School of Stomatology, The Fourth Military Medical University, Xi'an, PR China. [2]Department of Medical Microbiology and Parasitology, The Fourth Military Medical University, Xi'an, PR China. [3]Department of Paediatric Dentistry, School of Stomatology, China Medical University, Shenyang, PR China. [4]Stomatology Hospital, Southern Medical University, Guangzhou, PR China. [5]Department of Otolaryngology Head and Neck Surgery, Peking University Third Hospital, Beijing, PR China. [6]These authors contributed equally: Huijuan Kuang, Geng Dou. ✉e-mail: yanjin@fmmu.edu.cn; liushiyu@vip.163.com
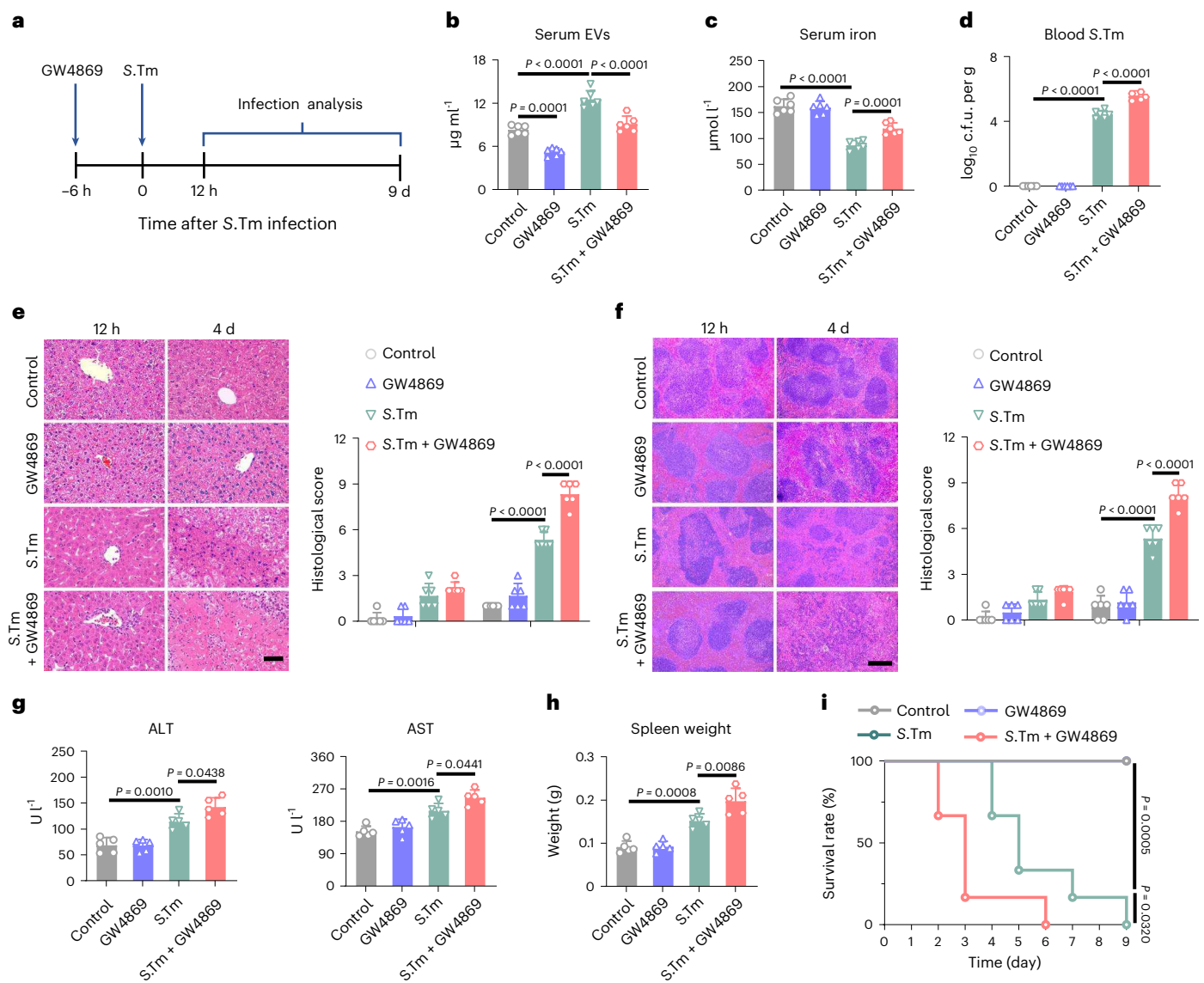
Fig. 1 | Blockade of host EV release increases the susceptibility of mice infected with S. Typhimurium. a, Schematic diagram of the experimental procedure. To evaluate the effects of EV release blockade on host defense response to infection, the uninfected or *S.* Typhimurium-infected mice were pretreated with GW4869. *S.*Tm, *S.* Typhimurium. **b–d**, Control mice, GW4869-treated mice, *S.* Typhimurium-infected mice and *S.* Typhimurium-infected mice pretreated with GW4869 were killed 12 h after *S.* Typhimurium infection for further analysis. The concentration of EVs in serum (**b**). *n* = 6 mice. Iron level in serum (**c**). *n* = 6 mice. Viable count of *S.* Typhimurium in the blood (**d**). *n* = 6

mice. c.f.u., colony-forming unit. **e**, Hematoxylin and eosin (H&E) staining of representative liver sections and the associated histological scores at 12 h or 4 d after infection. Scale bar, 50 μm. *n* = 6 mice. **f**, H&E staining of representative tissue sections of the spleen at 12 h or 4 d after infection and the associated histological scores. Scale bar, 250 μm. *n* = 6 mice. **g**, ALT and AST levels in the serum at day 4 after infection. *n* = 5 mice. **h**, Spleen weight at day 4 after infection. *n* = 5 mice. **i**, Survival rates of mice. *n* = 6 mice. Data are presented as mean ± s.d. (**b–h**). Statistical significance was assessed by one-way analysis of variance (ANOVA) with Tukey's post hoc test (**b–h**) and log-rank test (**i**).

metabolism. First, several studies have found that the number of circulating EVs is highly increased in response to bacterial infection[7,8]. In addition, circulating EVs are captured mainly by liver or spleen macrophages[9], which is consistent with the route of iron recycling by the host during bacterial infection. Moreover, EVs can inherit the membrane characteristics of their parent cells[10,11], which indicates that EVs released from liver or spleen macrophages may contain membrane receptors to bind iron-containing proteins. Notably, regarding physical properties, nanosized EVs show a high diffusion coefficient and a high surface-to-volume ratio, which is related to their superior adsorptive capacity. These properties facilitate the rapid diffusion of EVs to affect distant cells or tissues[12] and the protection of host cells by EVs serving as decoys that bind bacterial toxin[13]. Therefore, we hypothesize that EVs

released by the host could bind and preserve iron-containing proteins and then recycle them back to macrophages, serving as circulating humoral 'iron catchers' to prevent bacteria from iron acquisition.

In this study, we found that *Salmonella enterica* subsp. *enterica* serovar Typhimurium (*S.* Typhimurium) induces endoplasmic reticulum stress (ERS) in host macrophages and activates inositol-requiring enzyme 1α (IRE1α) signaling, triggering lysosomal dysfunction and promoting EV release. EVs bearing receptors such as TfR bind iron-containing proteins, prevent bacteria from iron acquisition and recycle iron to tissue-resident macrophages, ultimately protecting against infection. Taken together, these findings reveal a previously unknown humoral regulatory mechanism of iron metabolism during bacterial infection, broadening the knowledge of iron metabolism in

a cellular and humoral manner. The findings also reveal the role of EVs in nutritional immunity and suggest that the release and circulation of EVs could promptly regulate systemic iron metabolism.

Results

EVs drive iron sequestration and antibacterial response

Immediate restriction of iron has been viewed as a critical innate defense mechanism against bacterial infection[14]. We first confirmed changes in iron distributions in mice infected with *S.* Typhimurium, a Gram-negative bacterium that frequently causes microbial sepsis[15]. As expected, the numbers of *S.* Typhimurium increased quickly in blood after infection (Extended Data Fig. 1a) and the serum iron levels declined markedly, whereas hepatic and splenic iron levels significantly increased (Extended Data Fig. 1b), similar to previous studies showing an alteration in iron distributions after *S.* Typhimurium infection[16,17]. Notably, we found that the EV concentration in serum was upregulated at 3 h after infection and continued to increase within 24 h (Extended Data Fig. 1c), suggesting that immediate elevation of EV level is a feature of the host response to infection. To explore the biodistribution of serum EVs, the DiR-labeled EVs were intravenously (i.v.) injected into mice. Ex vivo fluorescent imaging revealed that most of the infused EVs homed to the liver or spleen (Extended Data Fig. 1d). Furthermore, confocal images showed that the infused EVs were mainly taken up by liver or spleen F4/80+ macrophages (Extended Data Fig. 1b,f). These data suggest that the biodistribution of circulating EVs is consistent with that of systemic iron after bacterial infection; however, the role of infection-induced host EV release in iron metabolism and infection outcomes is still unknown.

To answer this question, we used GW4869, which has been successfully utilized to inhibit EVs release in vitro and in vivo[18,19], to block host EV release during infection (Fig. 1a). We first showed that GW4869 treatment did not induce toxicity in wild-type mice (Supplementary Fig. 1). We then found that *S.* Typhimurium-induced elevation of circulating EVs was significantly inhibited in mice subjected to GW4869 pretreatment (Fig. 1b). Moreover, compared to *S.* Typhimurium-infected mice, serum iron levels significantly increased in *S.* Typhimurium-infected mice pretreated with GW4869 (Fig. 1c). We also found that after infection, the expression of the iron export protein ferroportin 1 (FPN1) was downregulated, whereas the expression of the iron storage protein ferritin heavy chain 1 (FTH1) was upregulated in the liver and spleen (Extended Data Fig. 2a). More notably, in the presence of infection, although GW4869 treatment did not affect the expression of FPN1 or FTH1 (Extended Data Fig. 2a), it caused a decrease in hepatic or splenic iron levels (Extended Data Fig. 2b). These findings demonstrate that blockade of EV release disrupts iron recycling in mice during infection.

Next, we investigated the effects of EV release blockade on the host defense response to infection. We found that, compared to *S.* Typhimurium-infected mice, the viable count of *S.* Typhimurium increased markedly in the blood (Fig. 1d), liver and spleen (Extended Data Fig. 2c) of *S.* Typhimurium-infected mice pretreated with GW4869. Histological examination of the liver showed inflammatory infiltration at 12 h after bacterial infection. Severe liver injury was found at 4 d

after *S.* Typhimurium infection compared to uninfected control mice, as shown by gross lesions accompanied by inflammatory infiltration and elevated histological scores (Fig. 1e). More notably, the infected mice pretreated with GW4869 showed large areas of extensive cellular necrosis with loss of hepatic architecture and more severe inflammatory cell infiltration (Fig. 1e). Next, morphological changes in the spleen were investigated. At 12 h after infection, no obvious histological alterations were observed in the spleen (Fig. 1g). At 4 d after infection, the spleens from the infected mice displayed a distinctly irregular histology and a significant loss of the distinct borders between the red and white pulp regions. Moreover, the infected mice pretreated with GW4869 exhibited more severe spleen injuries and elevated histological scores (Fig. 1f). Liver injury was also examined by measuring the levels of aspartate aminotransferase (AST) and alanine aminotransferase (ALT) in serum. Compared to uninfected control mice, *S.* Typhimurium-infected mice showed elevated levels of ALT and AST in the sera. Pretreatment with GW4869 significantly enhanced serum ALT and AST levels in the infected mice (Fig. 1g). Splenomegaly is common following bacterial infection. Accordingly, we found that *S.* Typhimurium infection increased the spleen weight, with a significant increase in spleen weights observed in the GW4869-pretreated group (Fig. 1h). As long-term mortality is associated with sustained injury, survival experiments were performed[20]. Compared to phosphate-buffered saline (PBS)-treated control mice, *S.* Typhimurium-infected mice or *S.* Typhimurium-infected mice pretreated with GW4869 showed 100% mortality, whereas GW4869 pretreatment greatly shortened mouse survival time (Fig. 1i). In addition, although GW4869 treatment in wild-type mice induced a decrease in the concentration of serum EVs (Fig. 1b), it did not affect serum iron levels (Fig. 1c) or cause bacterial infection (Fig. 1d). Additionally, wild-type mice treated with GW4869 showed normal hepatic (Fig. 1e) and splenic architecture (Fig. 1f) and ALT and AST levels (Fig. 1g), along with normal splenic weight (Fig. 1h) and survival rate (Fig. 1i). These results suggest that during infection, blockade of host EV release disturbs iron sequestration, increases iron availability and worsens the outcomes of infection.

We further investigated the role of host EVs in iron metabolism and infection defense. We first isolated EVs from the serum of uninfected or *S.* Typhimurium-infected mice by ultracentrifugation. The isolated EVs were positive for the EV markers CD63, CD81, TSG101 and Alix but lacked the mitochondrial marker calnexin (Fig. 2a). Nanoparticle tracking analysis (NTA) showed that more than 90% of EVs were within the 30–120 nm range and the mean size of EVs derived from the serum of uninfected mice or *S.* Typhimurium-infected mice was 110 nm and 116 nm, respectively (Fig. 2b). A typical circular or elliptical morphology was also visible in transmission electron microscopy (TEM) images (Fig. 2c). These data show that *S.* Typhimurium infection does not substantially affect the marker expression, size or shape of EVs in serum. Next, to investigate the functions of EVs, GW4869-pretreated infected mice were i.v. injected with EVs derived from uninfected or *S.* Typhimurium-infected mouse serum (Fig. 2d). Administration of EVs caused markedly decreased levels of iron in serum, especially in mice treated with EVs derived from infected mouse serum
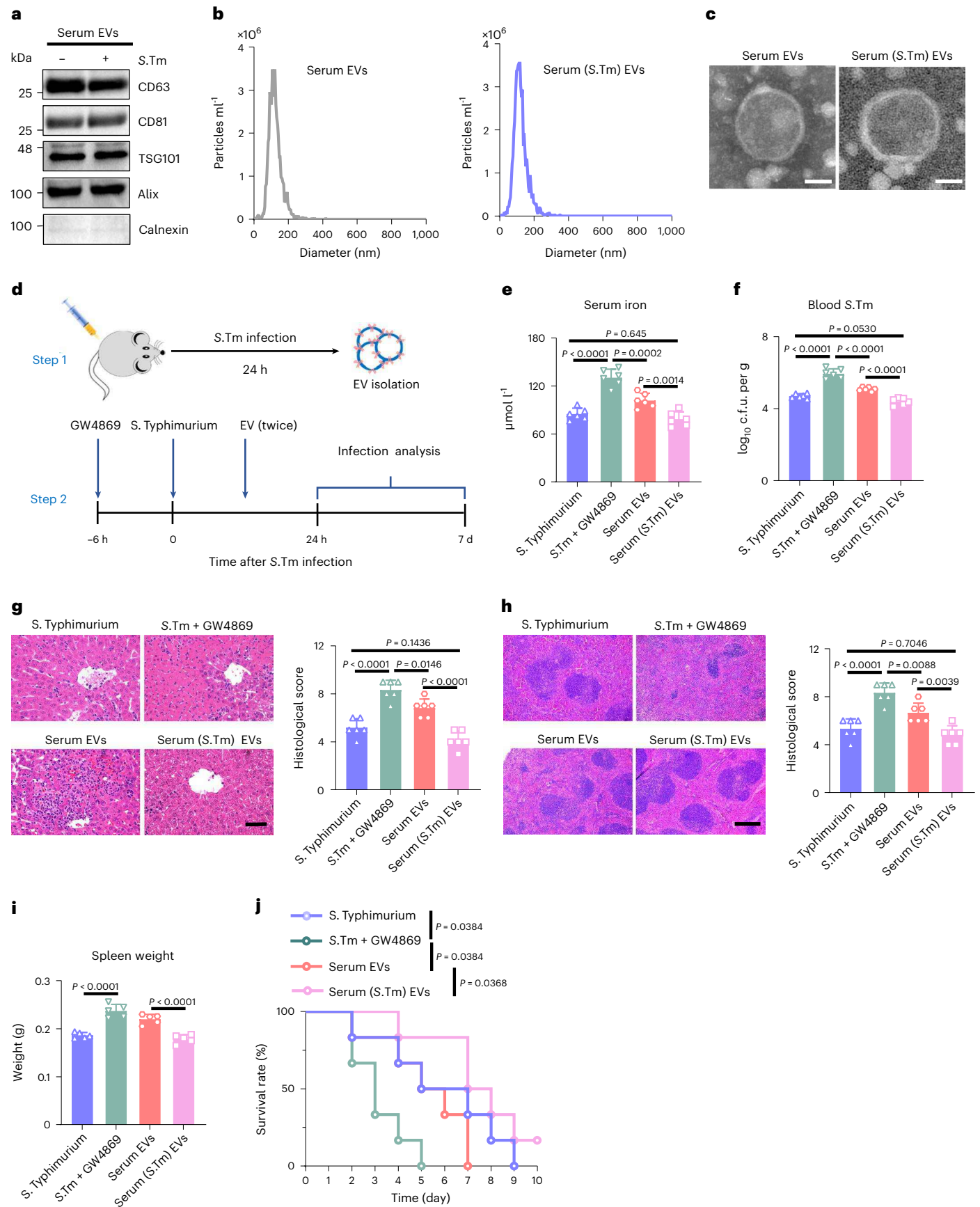
Fig. 2 | Supplementation with serum EVs decreases *S.* Typhimurium infection severity in EV-release-deficient mice. a–c, The mice were intraperitoneally injected with *S.* Typhimurium and the serum was collected after 24 h. EVs were isolated from uninfected mouse serum (serum EV group) or *S.* Typhimurium-infected mouse serum (serum (*S.* Typhimurium) EV group) and characterized. Western blot analysis of the EVs markers Alix, CD81, CD63 and TSG101 and the negative mitochondrial marker calnexin (**a**). Experiments were repeated three times and representative images are shown. NTA analysis of the concentration and size distribution of EVs (**b**). TEM analysis of EVs (**c**). Scale bar, 50 nm. *S.*Tm, *S.* Typhimurium. Experiments were repeated twice and representative images are shown. **d**, Schematic diagram of the in vivo experimental procedure. EVs were isolated from uninfected mouse serum or *S.* Typhimurium-infected

mouse serum (step 1). To investigate the role of host EVs in iron metabolism and infection outcomes, GW4869-pretreated *S.* Typhimurium-infected mice were injected with EVs derived from the serum EV group or EVs derived from the serum (*S.* Typhimurium) EV group (step 2). **e**, The iron level in serum after *S.* Typhimurium infection. *n* = 6 mice. **f**, Viable count of *S.* Typhimurium in blood after *S.* Typhimurium infection. *n* = 6 mice. **g,h**, Representative H&E staining of the liver (**g**) and spleen (**h**) at 4 d after *S.* Typhimurium infection and quantitative analysis of histological scores. Scale bar, 50 μm (**g**) and 250 μm (**h**). *n* = 6 mice. **i**, The spleen weight at 4 d after infection. *n* = 5 mice. **j**, Survival rate of mice. *n* = 6 mice. Data are presented as the mean ± s.d. (**e–i**). Statistical significance was assessed by one-way ANOVA with Tukey's post hoc test (**e–i**) and log-rank test (**j**).

(Fig. 2e). We also found that EV treatment resulted in a decreased number of bacteria in the blood (Fig. 2f), liver or spleen (Extended Data Fig. 2d,e), which was more evident in mice treated with EVs derived from infected mouse serum. Regarding histological analysis, at 4 d after infection, the *S*. Typhimurium-infected mice pretreated with GW4869 developed substantial liver (Fig. 2g) and spleen injury
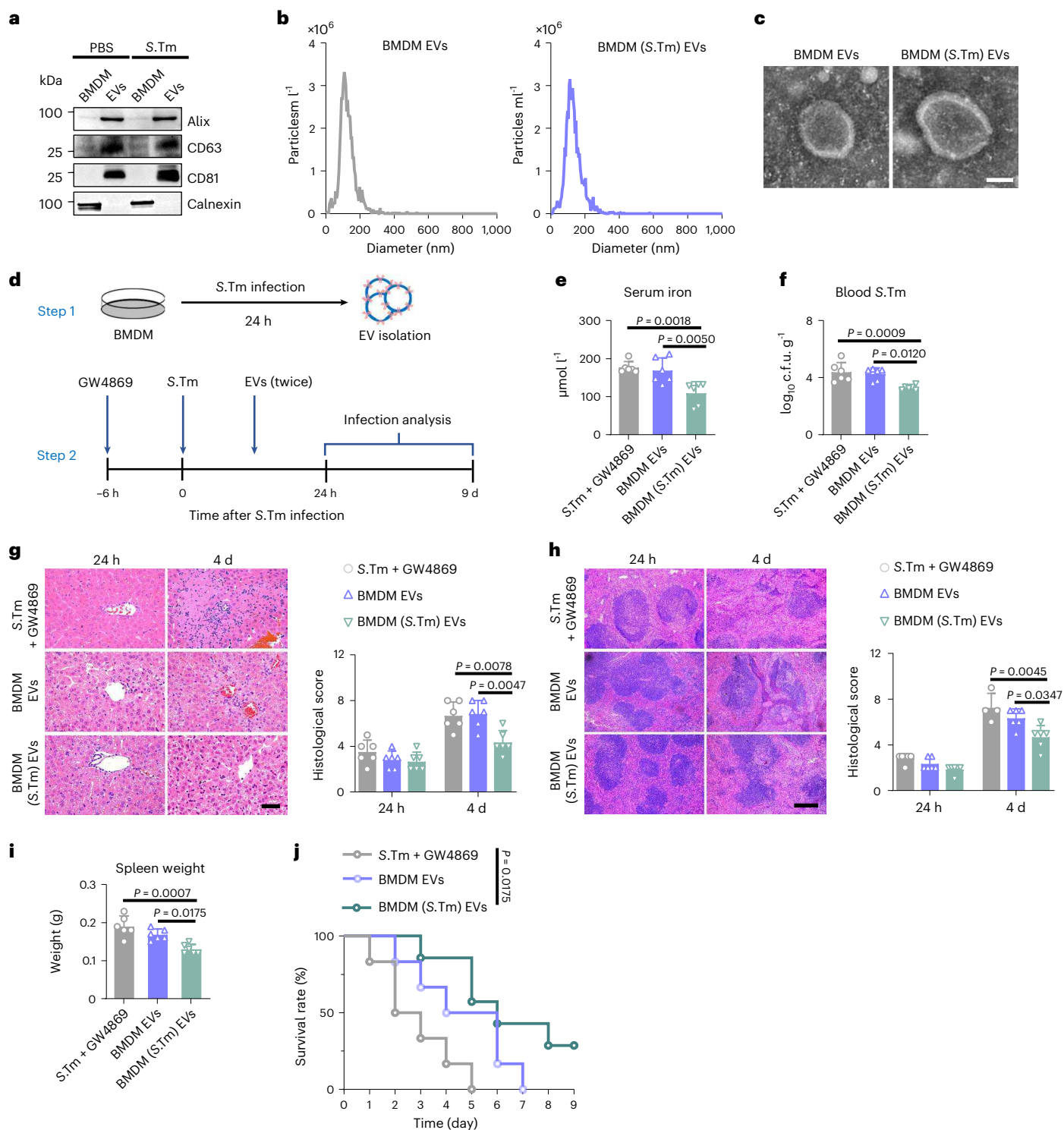
Fig. 3 | Supplementation with EVs derived from BMDMs decreases infection severity in EV-deficient mice. a–c, BMDMs were infected with *S*. Typhimurium for 24 h at a multiplicity of infection (m.o.i.) of 10. EVs were isolated from uninfected BMDMs (BMDM EV group) or *S*. Typhimurium-infected BMDMs (BMDM (*S*. Typhimurium) EV group) and characterized. *S*.Tm, *S*. Typhimurium. **a**, Western blot analysis of the EVs markers Alix, CD81, CD63 and TSG101 and the negative mitochondrial markers calnexin. Experiments were repeated three times and representative images are shown. **b**, NTA analysis of the concentration and size distribution of EVs. **c**, TEM images of EVs, scale bar, 50 nm. Experiments were repeated twice and representative images are shown. **d**, Schematic diagram of the experimental procedure. EVs were isolated from uninfected BMDM or *S*. Typhimurium-infected BMDMs (step 1). To investigate the role of host EVs in

iron metabolism and infection outcomes, GW4869-pretreated *S*. Typhimurium-infected mice were i.v. injected with EVs derived from the BMDM EV group or the BMDM (*S*. Typhimurium) EV group and mice were killed after 24 h for further analysis (step 2). **e**, Iron levels in serum. *n* = 6 mice. **f**, Viable count of *S*. Typhimurium in blood. *n* = 6 mice. **g,h**, Representative H&E staining of the liver (**g**) and spleen (**h**) at 24 h or 4 d after *S*. Typhimurium infection and quantitative analysis of histological scores. Scale bar, 50 μm (**g**) and 250 μm (**h**), *n* = 4–6 mice. **i**, Quantitative analysis of the spleen weights at day 4 after infection, *n* = 6 mice. **j**, Survival rate of mice, *n* = 6–7 mice. Data are presented as mean ± s.d (**e–i**). Statistical significance was assessed by one-way ANOVA with Tukey's post hoc test (**e–i**) and log-rank test (**j**).

(Fig. 2h); however, EV administration could ameliorate liver and spleen injury. In particular, compared to EVs from uninfected mouse serum, EVs from *S*. Typhimurium-infected mouse serum more effectively improved hepatopathological changes, such as liver injury area and inflammatory infiltration (Fig. 2g), alleviated pathological lesions in the spleen and improved splenic structure (Fig. 2h). Additionally, treatment with EVs derived from infected mouse serum significantly reduced liver (Fig. 2g) and spleen (Fig. 2h) injury scores and alleviated spleen enlargement (Fig. 2i). Notably, EV treatment also improved survival under sepsis. While most of the GW4869-pretreated septic mice died within 5 d, GW4869-pretreated septic mice treated with serum EVs had a higher survival rate, especially in the mice treated with EVs derived from *S*. Typhimurium-infected mouse serum (Fig. 2j). These data demonstrate that bacterial infection induces immediate release of EVs, facilitating prompt iron sequestration and protecting against bacterial infection.

We next investigated which kinds of cells could release EVs that have iron metabolism regulation functions. It has been proven that macrophages have a precise regulatory system to maintain iron homeostasis during bacterial infection[21]. Therefore, we utilized primary bone-marrow-derived macrophages (BMDMs) (Extended Data Fig. 3a), widely used as prototypical macrophages for in vitro studies[22], to investigate EV functions. Then, we isolated and characterized EVs from the supernatants of BMDMs treated with *S*. Typhimurium or PBS. Analysis of marker expression (Fig. 3a), particle size (Fig. 3b) and morphology (Fig. 3c) showed the isolated BMDM EV fractions and that *S*. Typhimurium infection did not alter the general properties of the EVs. Next, these EVs were systemically injected into infected mice pretreated with GW4869 (Fig. 3d). The serum iron levels declined markedly only in infected mice injected with EVs derived from *S*. Typhimurium-treated BMDMs (Fig. 3e). Concomitantly, the numbers of *S*. Typhimurium decreased markedly in blood (Fig. 3f). The administration of EVs derived from infected BMDMs reduced liver (Fig. 3g) and spleen (Fig. 3h,i) injury. Ultimately, the injection of EVs from infected BMDMs extended the survival of septic mice pretreated with GW4869 (Fig. 3j). These results demonstrate that EVs released by macrophages are involved in iron sequestration and protect against infection.

Host EVs bearing multiple iron-related receptors bind iron

We next determined how host EVs facilitate iron sequestration. During bacterial infection, macrophages take up iron or iron-containing molecules via receptors, including TfR, CD91 and CD163 receptors[23]. We found that compared to uninfected BMDMs, the expression levels of the iron-related receptors TfR, CD91, CD163 and FTH1 were significantly upregulated in *S*. Typhimurium-infected BMDMs (Extended Data Fig. 3b), whereas the expression of FPN1 was downregulated, leading to increased cellular iron content (Extended Data Fig. 3c). Given that we found that EVs released by *S*. Typhimurium-infected BMDMs participate in iron sequestration, we wondered whether EVs released by macrophages expressed these iron-related receptors and directly bound iron or iron-containing molecules. We hypothesized that EV-based iron sequestration could serve as an efficient strategy for prompt iron recycling during infection. We therefore isolated EVs from mouse serum and BMDM culture supernatants and measured iron-related receptor expression. We found that EVs derived from serum (Fig. 4a, left) or BMDMs (Fig. 4a, right) expressed TfR, CD91 and CD163, which were not changed by GW4869 treatment but were significantly upregulated after *S*. Typhimurium infection. Further determination of TfR, CD91 and CD163 localization was performed by immunoelectron microscopy[24] and the results showed that TfR, CD91 and CD163 were present on the surface of serum EVs (Fig. 4b) or BMDM-derived EVs (Fig. 4c).

Next, we determined whether these EVs bind iron or iron-containing molecules to sequester iron in serum to inhibit bacterial growth. EVs derived from infected or uninfected mouse serum were added to EV-depleted serum of GW4869-pretreated infected

mice. After incubation, the added EVs were isolated by ultracentrifugation and serum supernatant was collected for analysis of iron levels or for *S*. Typhimurium culture (Fig. 4d). The results showed that the addition of EVs derived from uninfected or *S*. Typhimurium-infected mouse serum induced a decrease in iron levels (Fig. 4e) and EVs from the infected mouse serum had higher iron-capture abilities, which may be because EVs derived from the infected mouse serum expressed higher levels of iron-related receptors (Fig. 4a, left) and could bind iron-containing molecules. In the host, iron exists in multiple forms including transferrin, ferritin, hemoglobin and other iron-containing proteins[25]. Transferrin is the major iron shuttle in the circulation[26] and is a critical source of iron for bacteria during infection[27]. Given that TfR expression in EVs from infected mice was significantly upregulated (Fig. 4a, left), we next determined the ability of EVs to bind transferrin. After EV incubation, transferrin concentration was decreased in the serum supernatant (Fig. 4f). The incubation of EVs derived from infected mouse serum caused a greater decrease in transferrin concentration (Fig. 4f). In addition, to further prove the binding ability of EVs, the added EVs were isolated and the transferrin level in the EV fraction was measured. The results showed that the transferrin level in EVs derived from infected mouse serum was significantly higher than that in EVs derived from uninfected mouse serum (Fig. 4g). These results demonstrate that EVs serve as 'iron catchers' via membrane-bearing receptors such as TfR. To further determine whether EVs could protect the captured iron from bacterial acquisition, EVs derived from infected mouse serum were incubated with *S*. Typhimurium. The fluorescence images showed rare uptake of EVs by *S*. Typhimurium (Fig. 4h), which indicated that *S*. Typhimurium could not directly acquire iron by EV uptake. Therefore, these data demonstrate that EVs can prevent bacteria from iron acquisition.

S. Typhimurium is a highly iron-dependent bacterial pathogen[28]. As EVs derived from infected mouse serum induced the significant decrease in iron and transferrin levels in serum supernatant (Fig. 4e,f), we then determined whether this serum supernatant is unfavorable for bacterial growth after EVs bind iron. Serum supernatant after incubation with EVs derived from uninfected or infected mouse serum was inoculated with *S*. Typhimurium (Fig. 4d) and significant differences in growth curves were observed, including in the overall pattern of the growth curve, lag phase and peak doubling time (Fig. 4i). We found that, compared to control serum, *S*. Typhimurium grew more slowly in serum supernatant that was incubated with EVs derived from uninfected or infected mouse serum (Fig. 4i), whereas supplementation with iron-dextran in this serum supernatant recovered *S*. Typhimurium growth (Fig. 4i). We then performed the same experiment to detect whether EVs derived from infected BMDMs had the ability to bind iron or iron-containing molecules. Additionally, to prove certain receptor-mediated iron binding, EVs derived from infected BMDMs were pretreated with excess holo-transferrin to saturate TfR. The results showed that EVs derived from infected BMDMs induced greater decreases in total iron (Fig. 4j) and transferrin (Fig. 4k) levels than EVs derived from uninfected BMDMs and the capturing capacity was attenuated by holo-transferrin blocking. Similarly, *S*. Typhimurium grew more slowly in the serum supernatant that was incubated with EVs derived from infected BMDMs (Fig. 4l), which was attenuated by holo-transferrin blocking. In addition, EVs derived from infected BMDMs induced a significant decrease in serum iron levels (Extended Data Fig. 4a) and the levels of *S*. Typhimurium in mice (Extended Data Fig. 4b), which could be attenuated by holo-transferrin blockade (Extended Data Fig. 4). These results suggest that EVs released during infection inhibit *S*. Typhimurium growth by binding iron.

We proved that iron-related receptors, including TfR, CD91 and CD163, were upregulated in EVs released from *S*. Typhimurium-infected mice or BMDMs, so we wondered whether this represents a general mechanism used by host cells to bind iron and limit iron access by bacteria. We next used Gram-positive *Staphylococcus aureus*, which
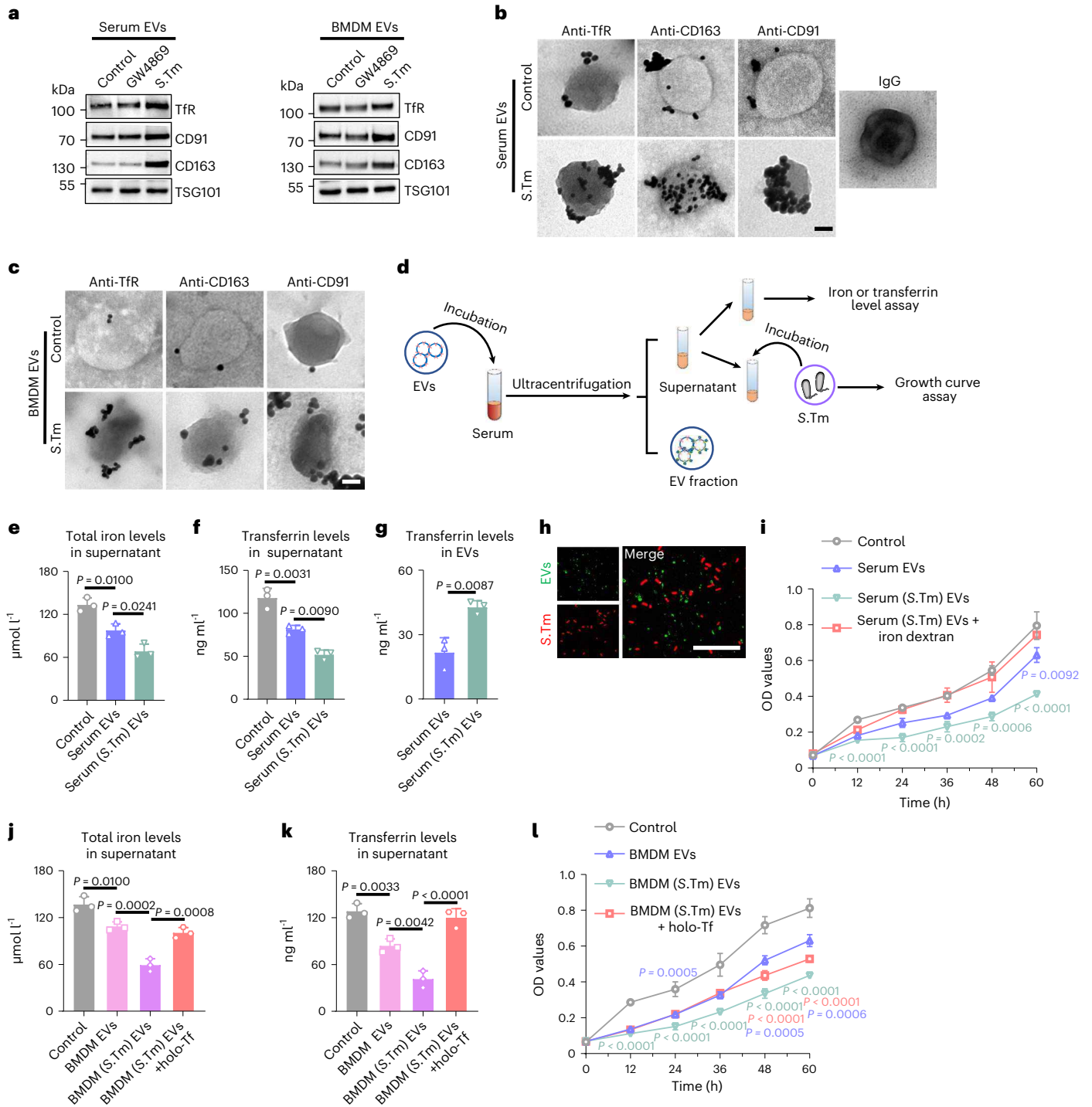
Fig. 4 | TfR-, CD163- and CD91-bearing EVs derived from *S.* Typhimurium-infected serum or BMDMs bind iron. a–c, Wild-type mice were intraperitoneally injected with *S.* Typhimurium and serum EVs were isolated after 24 h. BMDMs were infected with *S.* Typhimurium in vitro and supernatant EVs were isolated after 24 h. *S.*Tm, *S.* Typhimurium. **a**, Western blot analysis of TfR, CD163, CD91 and TSG101 expression in EVs derived from uninfected or infected mouse serum (left) and in EVs released from uninfected or infected BMDMs (right). Experiments were repeated three times and representative images are shown. **b**, Immunoelectron microscopy detection and isotype control IgG antibodies in EVs derived from uninfected or infected mouse serum. Scale bar, 50 nm. **c**, Immunoelectron microscopy detection of TfR, CD163 and CD91 in EVs derived from uninfected or infected BMDM. Scale bar, 50 nm. Experiments were repeated twice and representative images are shown (**b**,**c**). **d**, Schematic diagram of the experimental design to test the ability of EVs to bind iron in serum. EVs derived from uninfected mouse serum (serum EV group) or infected mouse serum (serum (*S.* Typhimurium) EV group) were used. **e**,**f**, Total iron (**e**) and transferrin levels (**f**) in the serum supernatant, *n* = 3 biologically independent samples. **g**, Transferrin levels in EV fractions derived from uninfected or infected mouse serum, *n* = 3 biologically independent samples. **h**, Representative fluorescence images of *S.* Typhimurium expressing mCherry (red) incubated with EVs (green) derived from infected mouse serum. Scale bars, 10 μm, *n* = 3 biologically independent samples. **i**, Growth curve of *S.* Typhimurium in serum supernatant, *n* = 3 biologically independent samples. **j**–**l**, To test the ability of EVs to bind iron in serum, uninfected BMDM-derived EVs (BMDM EV group), infected BMDM-derived EVs (BMDM (*S.* Typhimurium) EV group) or infected BMDM-derived EVs pretreated with excess holo-transferrin (BMDM (*S.* Typhimurium) EV + holo-Tf group) were used. Total iron levels (**j**) and transferrin levels (**k**) in serum supernatant, *n* = 3 biologically independent samples. Growth curve of *S.* Typhimurium in serum supernatant (**l**), *n* = 3 biologically independent samples. Data are presented as the mean ± s.d. (**e**-**g**,**i**-**l**). Statistical significance was assessed by one-way ANOVA with Tukey's post hoc test (**e**,**f**,**i**–**l**) and an unpaired two-tailed Student's *t*-test (**g**).

is an important cause of sepsis[29], to infect mice and BMDMs. Consistent with our findings, the expression levels of TfR, CD91 and CD163 in EVs derived from serum (Extended Data Fig. 5a, left) or BMDMs (Extended Data Fig. 5a, right) were all elevated after *S. aureus* infection. The immunoelectron microscopy images further confirmed the surface location of these receptors (Extended Data Fig. 5b). We also measured iron binding capacity of these EVs in serum (Extended Data Fig. 5c). Incubation with EVs derived from *S. aureus*-infected mouse serum induced a significant decrease in total iron (Extended Data Fig. 5d) and transferrin (Extended Data Fig. 5e) levels in serum supernatant. When the serum supernatant with lower iron levels was inoculated with *S. aureus* the growth rates were significantly decreased (Extended Data Fig. 5f). Therefore, we found that during bacterial infection, the levels of iron-related receptors including TfR, CD91 and CD163 in host EVs are elevated for prompt iron sequestration, demonstrating a humoral regulatory mechanism of iron metabolism.

EV-induced hypoferremia protects against infection

Although we found that EV release is required for prompt iron sequestration and resistance to infection and that EVs can bind iron-containing molecules, the protective effects generated by host EVs during infection still require further clarification. During infection, serum iron content is downregulated in a timely manner by the host to induce hypoferremia[30], which has been considered a critical defense mechanism to restrict iron availability to invading pathogens[31,32]. We then determined whether the iron-binding capability of EVs was involved in the development of rapid hypoferremia. To evaluate the protective effects of EVs induced by *S. Typhimurium* infection, we used heat-killed (HK) *S. Typhimurium* to induce host EV release while avoiding lethal virulence (Fig. 5a). HK *S. Typhimurium* has been proven to be recognized by the same mechanism as *Salmonella*[33]. We found that the concentration of serum EVs was increased after HK *S. Typhimurium* treatment (Extended Data Fig. 6a). The expression of iron-related receptors, including TfR, CD91 and CD163, was also upregulated in serum EVs after HK *S. Typhimurium* treatment (Extended Data Fig. 6b). These data indicate that the HK *S. Typhimurium*-induced EVs have iron-binding potential. As expected, compared to *S. Typhimurium*-infected mice, pretreatment with HK *S. Typhimurium* before *S. Typhimurium* infection led a significant increase in the number of EVs in serum (Fig. 5b). Moreover, infected mice pretreated with HK *S. Typhimurium* had a marked drop in serum iron (Fig. 5c) and decreased levels of *S. Typhimurium* in blood (Fig. 5d). Compared to the liver and spleen injury induced by *S. Typhimurium* infection, pretreatment with HK *S. Typhimurium* attenuated liver (Fig. 5e) and spleen injury (Fig. 5f), accompanied by a reduction in injury scores. Pretreatment with HK *S. Typhimurium* also significantly reduced *S. Typhimurium*-induced splenomegaly (Fig. 5g). In addition, most notably, compared to *S. Typhimurium*-infected mice, infected mice that received HK *S. Typhimurium* pretreatment lived significantly longer (Fig. 5h). To further clarify the association between the protective effect and EV release, we used GW4869 to inhibit EV release

(Fig. 5b). GW4869 treatment significantly attenuated the downregulation of serum iron levels by HK *S. Typhimurium* pretreatment (Fig. 5c), which subsequently resulted in an increase in *S. Typhimurium* levels in blood (Fig. 5d). Blockade of EV release by GW4869 also strongly attenuated HK *S. Typhimurium*-mediated protection in infected mice, including liver (Fig. 5e) and spleen (Fig. 5f,g) injury. Notably, compared to infected mice pretreated with HK *S. Typhimurium*, GW4869 treatment significantly shortened survival (Fig. 5h). The above results demonstrate that during infection, elevated EV levels cause prompt hypoferremia, which contributes to host defense against infection.

To further evaluate the protective effects of EVs induced by HK *S. Typhimurium*, we used an iron overload infection model established through iron-dextran injection and *S. Typhimurium* infection (Fig. 5i). The results showed that, compared to *S. Typhimurium*-infected mice, iron-dextran treatment contributed to high levels of *S. Typhimurium* in blood (Fig. 5j), which induced more extensive necrosis in the liver, disturbed architecture in the spleen, elevated histological injury scores of the liver and spleen (Fig. 5k), aggravated splenomegaly (Fig. 5l) and shortened survival (Fig. 5m). The administration of EVs resulted in a decreased number of bacteria in the blood (Fig. 5j), ameliorated liver and spleen injury (Fig. 5k), alleviated spleen enlargement (Fig. 5l) and prolonged survival time (Fig. 5m). Taken together, these results demonstrate that host EVs are released into the circulation to trigger prompt iron sequestration and hypoferremia and consequently restrict iron accessibility and protect against infection.

To further explore the role of macrophage EV release during infection, mouse macrophages were depleted by liposome-encapsulated clodronate (Extended Data Fig. 7a) and mice were injected i.v. with BMDMs, Rab27a short hairpin (sh)RNA-transfected BMDMs or an equal volume of PBS before *S. Typhimurium* infection. Rab27a has been shown to participate in EV release[34]. The results showed that clodronate treatment suppressed *S. Typhimurium*-induced EV release, which was restored by the adoptive transfer of BMDMs (Extended Data Fig. 7b); however, adoptive transfer of Rab27a shRNA-transfected BMDMs led to attenuated restoration of EV release (Extended Data Fig. 7b). Consistent with the EV concentration changes, serum iron (Extended Data Fig. 7c), blood *S. Typhimurium* number (Extended Data Fig. 7d) and survival rate (Extended Data Fig. 7e) in groups with different treatments further confirm the conclusion that EVs enhance host iron recycling, inhibit bacterial growth and finally facilitate survival. We also depleted macrophages before HK *S. Typhimurium* treatment and demonstrated the critical role of macrophages in EV release induced by infection (Extended Data Fig. 7f). These results demonstrate that macrophages play a critical role in host EV release and antibacterial response during bacterial infection.

ER stress-induced lysosomal dysfunction increases EV release

Given that we have identified a role of host EV release during infection, we next determined how bacterial invasion induces EV release. EVs are generated by fusion of multivesicular bodies with the plasma

Fig. 5 | Host EV-induced hypoferremia protects against bacterial infection. a, Schematic diagram of the experimental procedure. To evaluate the protective effects of EVs induced by *S. Typhimurium*, *S. Typhimurium*-infected mice were pretreated with HK *S. Typhimurium* to induce host EV release (HK *S. Typhimurium* + *S. Typhimurium* group). Additionally, to elucidate the association between EV release and the protective effect, *S. Typhimurium*-infected mice were pretreated with GW4869 in the absence (GW4869 + *S. Typhimurium* group) or the presence of HK *S. Typhimurium* (GW4869 + HK *S. Typhimurium* + *S. Typhimurium* group). Mice received injections of PBS as a control. *S*.Tm, *S. Typhimurium*. **b**, Concentration of EVs in serum at 12 h after *S. Typhimurium* infection, $n = 6$ mice. **c**, Iron level in serum at 12 h after *S. Typhimurium* infection, $n = 6$ mice. **d**, Viable count of *S. Typhimurium* in blood 12 h after *S. Typhimurium* injection, $n = 6$ mice. **e,f**, Representative H&E staining of the liver (**e**) or spleen (**f**) at day 4 after *S. Typhimurium* infection and

histological scores. Scale bar, 50 μm (**e**) and 250 μm (**f**), $n = 6$ mice. **g**, The spleen weight at day 4 after *S. Typhimurium* infection, $n = 5$ mice. **h**, Survival rates of mice, $n = 6$ mice. **i**, Schematic diagram of the experimental procedure. EVs were isolated from HK *S. Typhimurium*-treated mouse serum (step 1). To determine the protective effect of EVs induced by HK *S. Typhimurium*, iron-loaded mice were injected with EVs at −6, 0 and 6 h after *S. Typhimurium* infection (step 2). **j**, Viable count of *S. Typhimurium* in blood 24 h after *S. Typhimurium* injection, $n = 6$ mice. **k**, Representative H&E staining of the liver (upper) and spleen (bottom) at day 3 after *S. Typhimurium* infection and histological scores. Scale bar, 50 μm (top) and 250 μm (bottom), $n = 6$ mice. **l**, The spleen weight at day 3 after infection, $n = 6$ mice. **m**, Survival rates of mice, $n = 6$ mice. Data are represented as mean ± s.d. (**b–g,j–l**). Statistical significance was assessed by one-way ANOVA with Tukey's post hoc test (**b–g,j–l**) and log-rank test (**h,m**).

membrane[35]. In addition to exocytosis, multivesicular bodies can also fuse with lysosomes to generate phagolysosomes for degradation[35]. Strong evidence shows that lysosomal dysfunctions caused by various conditions result in increased exocytosis and EV release[35]. Here, we found reduced lysosome acidity by LysoTracker (fluorescent acidic organelle tracer) and cathepsin probe (Magic Red) in macrophages
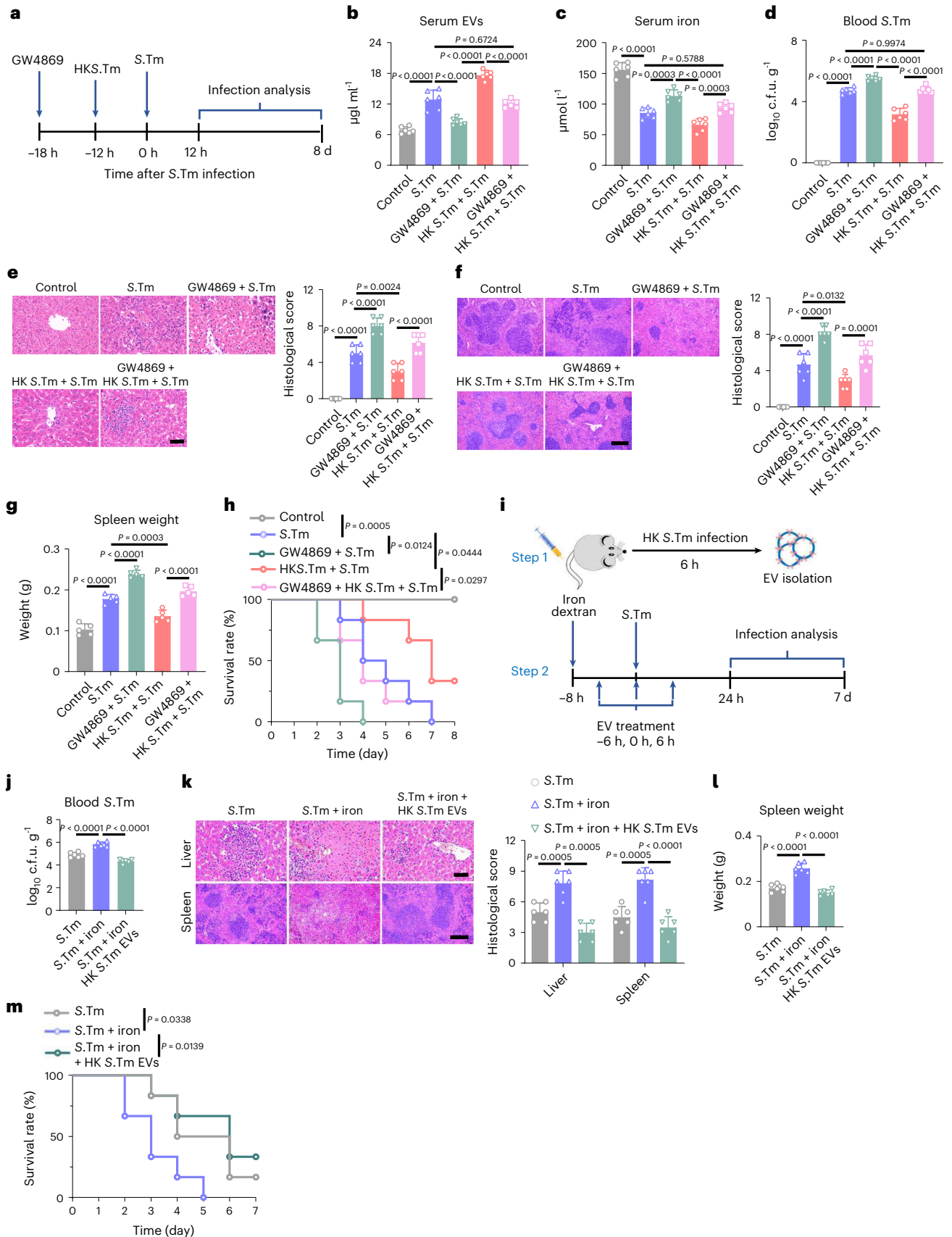
after *S*. Typhimurium infection in vitro (Fig. 6a), which may account for the enhanced EV release. More evidence provided by western blot showed reduced expression of ATP6V1A and ATP6V1B, subunits of V-ATPase, in macrophages after *S*. Typhimurium infection (Fig. 6b), which confirmed the lysosomal dysfunction caused by *S*. Typhimurium infection. Additionally, we used the mTOR activity inhibitor Torin-1 to restore lysosomal activity in the presence of *S*. Typhimurium infection. As expected, Torin-1 treatment restored lysosomal functions, as indicated by the restored lysosomal acidity and activity (Fig. 6a) and ATP6V1A/B expression (Fig. 6b). Moreover, Torin-1 treatment attenuated the *S*. Typhimurium infection-induced promoting effects on EV release (Fig. 6c). To further clarify the relationship between lysosomal function and EV release, we used the V-ATPase inhibitor bafilomycin A to induce lysosomal dysfunction. As expected, bafilomycin A markedly inhibited lysosomal acidity (Fig. 6a) and promoted EV release (Fig. 6c), generating effects similar to those of *S*. Typhimurium infection. Hence, the results demonstrate that the lysosomal dysfunction caused by infection promotes EV release (Fig. 6a–c).

We then investigated how bacterial invasion induces lysosomal dysfunction and EV release. Lysosomal function has been shown to be closely associated with endoplasmic reticulum stress (ERS)[35], which is activated when cells are subjected to bacterial infection[36]; however, whether ERS caused by bacterial infection controls EV release by regulating lysosome function has not yet been elucidated. Therefore, we first explored whether ERS was triggered and could regulate lysosomal function in infected macrophages. We found tremendous intracellular reactive oxygen species (ROS) caused by *S*. Typhimurium stimulation (Fig. 6d). In addition, TEM images showed *S*. Typhimurium infection-induced morphological dilatation of the endoplasmic reticulum (Fig. 6e). At the same time, the expression of ERS-related proteins, including IRE1α, ATF4, ATF6 and GRP78, was evidently upregulated after infection (Fig. 6f), which was also evidenced by fluorescence images (Fig. 6g). The elevated intracellular calcium concentration indicated by fluorescence detection also confirmed ERS in infected macrophages (Fig. 6h,i). To clarify the association between ERS and lysosomal function, we used the ERS inhibitor 4-phenylbutyric acid (4-PBA)[37] to inhibit the ERS response after infection. TEM images showed that 4-PBA treatment significantly inhibited dilatation of the endoplasmic reticulum in *S*. Typhimurium-treated macrophages (Fig. 6e). Additionally, 4-PBA treatment effectively attenuated the upregulated expression of IRE1α, ATF4, ATF6 and GRP78 (Fig. 6f,g) and elevated Ca^{2+} levels (Fig. 6h,i) caused by bacterial infection, which substantiated the ERS inhibition effects of 4-PBA. Notably, 4-PBA treatment rejuvenated lysosomal acidity in *S*. Typhimurium-treated macrophages, as evidenced by fluorescence images (Fig. 6j) and fluorescence optical density (OD) value (Fig. 6k). In addition to lysosomal functions, LAMP1 staining showed that the lysosome number was obviously reduced in *S*. Typhimurium-treated macrophages, which was

also reversed by 4-PBA (Fig. 6l). Moreover, the decreased expression of ATP6V1A, ATP6V1B and LAMP1 was recovered after 4-PBA treatment (Fig. 6m). We also found that the level of TFEB, an important transcription factor that controls lysosomal biogenesis and function[38], was reduced after infection but was partially reversed after 4-PBA treatment (Fig. 6m). Finally, ERS inhibition attenuated the elevated EV release in macrophages induced by *S*. Typhimurium infection (Fig. 6n). These results demonstrate that ERS triggered by *S*. Typhimurium infection induced lysosomal dysfunction, thereby increasing EV release.

We also determined whether the above mechanism functioned in *S. aureus* infection. Similarly, the intracellular generation of ROS induced by *S. aureus* infection was observed (Extended Data Fig. 8a), accompanied by dilated endoplasmic reticulum (Extended Data Fig. 8b), increased expression of ERS-related proteins (Extended Data Fig. 8c,d) and enhanced intracellular Ca^{2+} levels (Extended Data Fig. 8e,f). These ERS effects generated by *S. aureus* could be abolished by 4-PBA treatment (Extended Data Fig. 8b–f). Moreover, ERS inhibition attenuated the elevated EVs release in macrophages induced by *S. aureus* infection (Extended Data Fig. 8g). Thus, these results suggest that the mechanism by which ERS-triggered lysosomal dysfunction induces host EVs release may generally function in bacterial infection.

IRE1α-mediated lysosomal dysfunction triggers EV release

After determining that ERS induced by bacterial infection causes lysosome dysfunction, we then explored the specific pathway that mediates this effect. IRE1α is one of the main transmembrane ERS sensors that initiates the downstream unfolded protein response pathway[35]. We then focused on the IRE1α pathway in lysosome function regulation based on our results, which showed upregulated IRE1α expression after infection (Fig. 6f). To verify the role of IRE1α in this mechanism, we inhibited IRE1α expression in macrophages with IRE1α short interfering (si)RNA or the pharmacological inhibitor toyocamycin. We found that the expression of IRE1α and activation of the downstream Erk pathway[39] were evidently decreased in infected macrophages after treatment with IRE1α siRNA (Fig. 7a) or toyocamycin (Fig. 7b). Moreover, inhibition of IRE1α by siRNA or toyocamycin was accompanied by an increase in the levels of TFEB, LAMP1, ATP6V1A and ATP6V1B, which suggested that lysosomal function was partially recovered (Fig. 7a,b). It has been proven that the activity of TFEB is strictly regulated through phosphorylation by Erk1/2, which inhibits the translocation of TFEB to the nucleus, where it increases the transcription of multiple genes implicated in lysosomal biogenesis, autophagy and exocytosis[38,40,41]. Therefore, we propose the hypothesis that macrophages develop ERS after bacterial infection and the downstream IRE1α pathway activates Erk1/2, resulting in TFEB inactivation and decreased lysosome biogenesis and function, finally promoting EV release. To confirm the mechanistic hypothesis, lysosomal function was further investigated in infected macrophages by fluorescence imaging. The results showed

---

Fig. 6 | *S*. Typhimurium infection induces host EV release via ERS-mediated lysosomal dysfunction. a–c, BMDMs were treated with *S*. Typhimurium in the absence or presence of Torin-1 for 24 h to detect lysosome function and EV release. Bafilomycin A was used as a positive control of lysosomal dysfunction. *S*.Tm, *S*. Typhimurium. **a**, Representative images of LysoTracker (green) and Magic Red (Red) staining detected by laser scanning confocal microscopy and the quantitative fluorescence intensity. AU, arbitrary units. Scale bar, 5 μm, *n* = 3 biologically independent samples. **b**, Western blot analysis. **c**, The concentration of EVs released by BMDMs was detected by NanoSight, *n* = 3 biologically independent samples. **d**, Representative fluorescence images of ROS in BMDMs infected with *S*. Typhimurium and quantitative analysis. Scale bar, 50 μm, *n* = 3 biologically independent samples. **e–n**, BMDMs were treated with *S*. Typhimurium in the absence or presence of 4-PBA for 24 h. The ultrastructural morphology of the endoplasmic reticulum was investigated via TEM (**e**). Scale bar, 1 μm. The white arrow indicates the endoplasmic reticulum. Western blot analysis (**f**). Representative fluorescence images of GRP78 in

BMDMs and quantitative analysis (**g**). Scale bar, 10 μm, *n* = 3 biologically independent samples. Representative fluorescence images of intracellular Ca^{2+} and quantitative analysis (**h**). Scale bar, 4 μm, *n* = 3 biologically independent samples. Intracellular Ca^{2+} level measured by microplate reader, *n* = 3 biologically independent samples (**i**). Representative images of LysoTracker (green) and Magic Red (Red) staining were detected by laser scanning confocal microscopy and the quantitative fluorescence intensity (**j**). Scale bar, 5 μm, *n* = 3 biologically independent samples. The fluorescence intensity of LysoTracker was detected by a microplate reader, *n* = 3 biologically independent samples (**k**). Fluorescence images of LAMP1 in BMDMs and quantitative analysis. Scale bar, 5 μm, *n* = 3 biologically independent samples (**l**). Western blot analysis (**m**). The concentration of EVs released by BMDMs were detected by NanoSight (**n**), *n* = 3 biologically independent samples. Data are represented as mean ± s.d. (**a,c,d, g–l,n**). Statistical significance was assessed by one-way ANOVA with Tukey's post hoc test (**a,c,g–l,n**) and unpaired two-tailed Student's *t*-test (**d**). All western blots were repeated three times and representative images are shown.

---

that the reduced lysosomal acidity (Fig. 7c,d) and decreased lysosome number (Fig. 7e) induced by *S*. Typhimurium infection was reversed after treatment with IRE1α siRNA or toyocamycin. More notably, the increased EV release caused by bacterial infection was also attenuated

(Fig. 7f). Thus, these results support the mechanism by which IRE1α in ERS induces lysosomal dysfunction, which then triggers EV release.

Finally, we determined the role of ERS in lysosomal dysfunction-induced EV release and iron metabolism in vivo. To
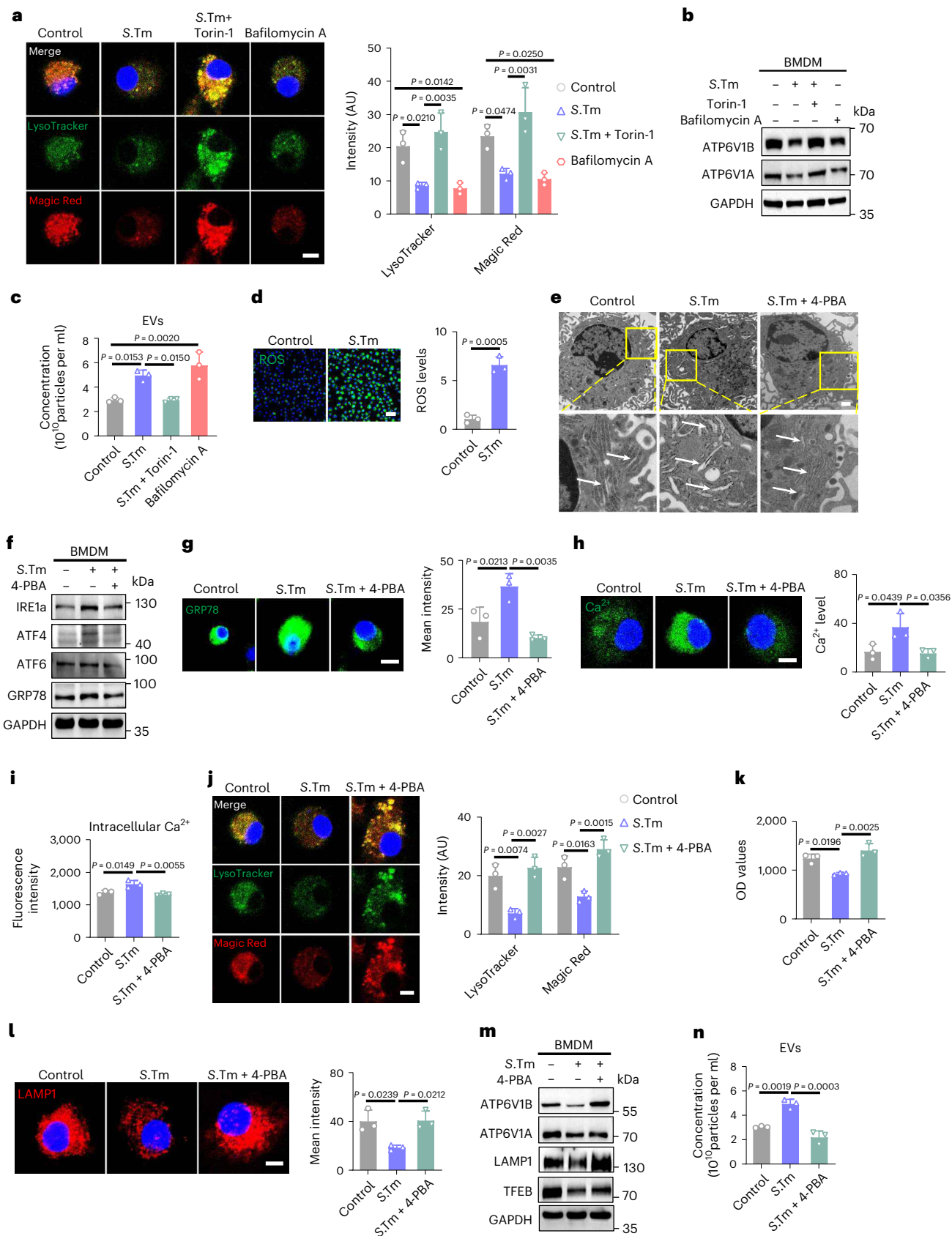
enhance the pharmacological effects of the ERS inhibitor 4-PBA in vivo, liposome-encapsulated 4-PBA was prepared, as liposomes are mainly taken up by macrophages in the liver or spleen[42]. The drug-loading efficiency of 4-PBA in liposomes was 89.3 ± 0.13%. Fluorescence imaging showed that infused rhodamine B (RhB)-labeled liposome-encapsulated 4-PBA could be effectively transported into the liver (Extended Data Fig. 9a) and engulfed by F4/80+ macrophages in vivo (Extended Data Fig. 9b) or in vitro (Extended Data Fig. 9c). Subsequently, *S*. Typhimurium-infected mice were treated with liposome-encapsulated 4-PBA to suppress ERS in vivo (Fig. 7g). We found that *S*. Typhimurium infection upregulated the expression of ERS-related proteins, including IRE1α, ATF6 and GRP78 in the liver (Fig. 7h). Additionally, fluorescence images showed that the number of F4/80+/GRP78+ macrophages increased significantly in the liver after infection (Fig. 7i). The 4-PBA treatment inhibited the expression of ERS-related proteins (Fig. 7h) and decreased the number of F4/80+/GRP78+ liver macrophages (Fig. 7i). The results demonstrated that 4-PBA attenuated *S*. Typhimurium-induced ERS in the liver. More notably, 4-PBA treatment decreased the concentration of serum EVs (Fig. 7j) and elevated iron levels in infected mice (Fig. 7k), which indicated that ERS inhibition attenuated iron sequestration by the host. Finally, we found that 4-PBA-treated infected mice exhibited higher blood bacterial numbers (Fig. 7l), serious injury to the liver (Fig. 7m) and spleen (Fig. 7n) accompanied by higher injury scores and a shortened lifespan (Fig. 7o). Thus, during infection, ERS development in host cells is required for EV release to realize iron sequestration and infection defense.

As we found that the infection enhanced the enrichment of iron-related receptors on EVs, we continued to explore whether ERS also functions in this process. The results showed that when 4-PBA was used to inhibit ERS in the presence of infection, the expression of iron-binding receptors on EVs significantly decreased (Extended Data Fig. 10a). Then we found that the expression level of Rab31, a GTPase family number, was significantly upregulated in macrophages after *S*. Typhimurium infection (Extended Data Fig. 10b). After knockdown of Rab31 expression in *S*. Typhimurium-infected macrophages, the expressions of iron-binding receptors on EVs was downregulated (Extended Data Fig. 10c), but EV production was not significantly changed (Extended Data Fig. 10d), demonstrating that Rab31 mediates the enrichment of iron-binding receptors on EVs. As we found that the expression of iron-binding receptors on EVs was downregulated after ERS inhibition (Extended Data Fig. 10a) and that Rab31 expression was also downregulated after ERS inhibition (Extended Data Fig. 10e), we wondered whether Rab31 acted downstream of the ERS–IRE1α pathway to enhance enrichment of the receptors. We then reduced IRE1α expression with siRNA knockdown or pharmacological inhibition in *S*. Typhimurium-infected macrophages (Extended Data Fig. 10f,g). The results showed that when the IRE1α level was inhibited, the Rab31 level was also decreased (Extended Data Fig. 10f,g). Moreover, the IRE1α expression inhibition reduced the enrichment of iron-binding

receptors on EVs (Extended Data Fig. 10h,i). These results indicated that *S*. Typhimurium infection induces ERS and activation of the IRE1α pathway and Rab31, downstream of IRE1α, mediates the enrichment of iron-binding receptors on EVs.

Taken together, the findings of this study reveal how host EVs facilitate immediate iron sequestration via a humoral regulation mechanism of iron metabolism. We found that *S*. Typhimurium infection induces ERS and activates IRE1α signaling in macrophages, resulting in lysosomal dysfunction and immediate EV release. These TfR-, CD163- and CD91-bearing EVs recycle iron to tissue-resident macrophages by binding iron-containing molecules for prompt iron sequestration (Fig. 8). Therefore, we identified a previously unknown humoral regulatory mechanism of iron metabolism during bacterial infection, revealed the role of EVs in nutritional immunity and suggested that the release and circulation of EVs could promptly regulate systemic ion metabolism.

Discussion

Iron is needed to fulfill multiple biological functions in living organisms due to its unique chemical properties[43]. Iron in host cells also acts as a signal to induce the generation of hydroxyl radicals and therefore kill intracellular pathogens[44,45]. Unsurprisingly, given its remarkable versatility and critical functions in biological systems, fierce competition for iron between the host and pathogen takes place under infection conditions. Successful invaders launched highly efficient machinery, including siderophore and hemophore systems, to capture iron from host iron sources[46]. To effectively inhibit the growth of bacterial pathogens, the host simultaneously evolves sophisticated defense mechanisms that restrict iron availability for bacterial pathogens and thereby limit their infection. The host employs siderophilins, including transferrin and lactoferrin, to transport iron to storage sites to limit iron uptake by the bacteria[47]. Moreover, host cells can release lipocalin-2 to obstruct the iron-acquiring strategy of bacteria[48]. Given that iron-containing proteins existing in body fluid can be acquired by the bacteria[2], it is important to explore how the host promptly acquires and preserves iron for rapid iron sequestration after infection.

For every tactic employed by invading pathogens to acquire iron, the host evolves relevant defense mechanisms. Notably, recent studies show that bacterial pathogens can release EVs such as outer membrane vesicles to acquire iron from their hosts. Outer membrane vesicles carry degradative enzymes and specific receptors that enable bacteria to efficiently acquire iron and thus to facilitate bacterial survival[49]. Therefore, it is worth considering whether the intelligent host has also developed a similar strategy to enhance the efficiency of iron sequestration by arranging decoys in the circulation. It has been proven that the total number of EVs is significantly increased during bacterial infection[13,50]. While most of the studies on EVs in bacterial infection have focused on the mechanisms for antigen presentation or signal transduction[51], other biological functions of EVs still need to be explored. A recent study provided evidence to support that EVs confer a benefit or survival advantage to their parental cells by serving

Fig. 7 | IRE1α-mediated lysosomal dysfunction enhances EV release during *S*. Typhimurium infection. a–f, To inhibit the expression of IRE1α, BMDMs were pretreated with IRE1α siRNA or toyocamycin and then infected with *S*. Typhimurium for 24 h. *S*.Tm, *S*. Typhimurium. Western blot analysis (**a**,**b**). Representative fluorescence images (**c**) and fluorescence intensity (**d**) of LysoTracker were detected by laser scanning confocal microscopy and a microplate reader, respectively. Scale bar, 5 μm, *n* = 3 biologically independent samples. Representative fluorescence images of LAMP1 in BMDMs and quantitative analysis of fluorescence intensity (**e**). Scale bar, 5 μm, *n* = 3 biologically independent samples. The concentration of EVs released by BMDMs was detected by NanoSight, *n* = 3 biologically independent samples (**f**). **g**, Schematic diagram of the experimental procedure. To verify the effects of ERS on lysosomal dysfunction-induced EV release and iron metabolism in vivo, empty liposomes or 4-PBA-encapsulated liposomes were injected intraperitoneally

into mice 6 h after intraperitoneal infection with *S*. Typhimurium. After 12 h, mice were killed for further analysis. **h**, Western blot analysis. **i**, Representative fluorescence images of GRP78 level in hepatic F4/80+ macrophages and quantification of the number of F4/80+/GRP78+ cells, *n* = 3 biologically independent samples. **j**, Concentration of EVs in the serum, *n* = 6 mice. **k**, Iron levels in serum, *n* = 6 mice. **l**, Viable counts of *S*. Typhimurium in the blood, *n* = 6 mice. **m**,**n**, Representative H&E staining of the liver (**m**) and spleen (**n**) after 4-PBA injection and quantitative analysis of histological scores. Scale bar, 50 μm (**m**) and 250 μm (**n**), *n* = 6 mice. **o**, Survival rates of mice, *n* = 5 mice. Data are represented as mean ± s.d. (**c**–**f**,**i**–**n**). Statistical significance was assessed by one-way ANOVA with Tukey's post hoc test (**c**–**f**,**i**–**l**), unpaired two-tailed Student's *t*-test (**m**,**n**) and log-rank test (**o**). All western blots were repeated three times and representative images are shown.

as decoys to trap and neutralize bacterial toxins[13]. This study suggests that EVs can exert their biological functions by specific membrane receptor binding capacity. Here, we found that host cells immediately release EVs to bind iron after infection, prevent bacteria from

iron acquisition and deliver iron to tissue-resident macrophages for prompt iron sequestration. The findings of our study reveal a previously unknown humoral regulatory mechanism of iron metabolism during bacterial infection, broadening the knowledge of iron
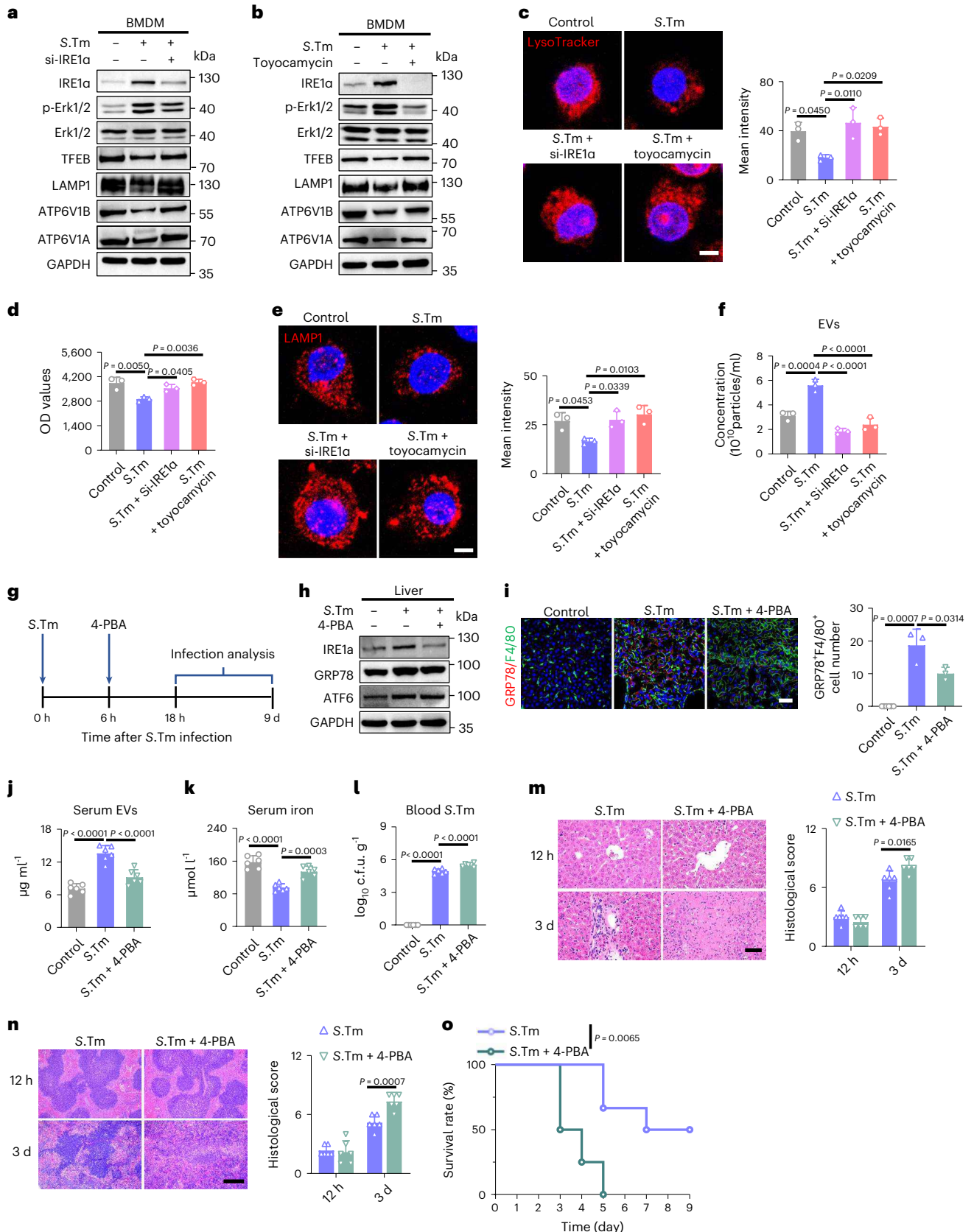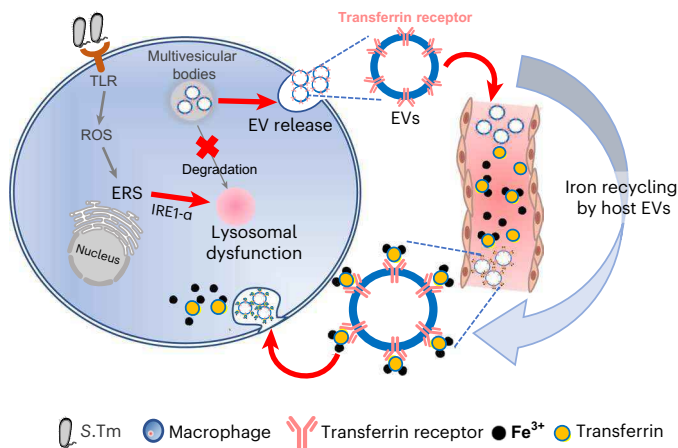
Fig. 8 | A humoral mechanism that promptly regulates systemic iron metabolism during bacterial infection. This work describes that upon bacterial invasion, host macrophages immediately release EVs that capture circulating iron-containing proteins to prevent bacteria from iron acquisition and ultimately protect against infection. *S*.Tm, *S*. Typhimurium.

metabolism in a cellular and humoral manner. Moreover, the findings show that host cells send circulating 'weapons' to compete with bacteria for iron, suggesting the evolutionarily conserved functions of EVs for iron acquisition in both prokaryotes and eukaryotes. To inhibit EV release in vivo, we used GW4869, which is the most widely used pharmacological agent for blocking EV generation[52] and is able to inhibit EV release in many kinds of cells, including mesenchymal stem cells[52], macrophages[52], hepatocytes[53], astrocytes[54], T cells[55], epithelial cells[56] and fibroblasts[52]. Given the potential side effects of GW4869, to determine the role of macrophage EV release in antibacterial response, mice were treated by clodronate for macrophage depletion and were supplemented with normal BMDMs or EV-release-deficient BMDMs before infection. The results demonstrate the critical role of macrophage EV release in iron metabolism and antibacterial response during infection.

EV release in host cells is ubiquitous and critical for an assortment of physiological and pathological processes[57]. EVs contain a broad array of biomolecules, including proteins, lipids and nucleic acids[57]. These nanosized EVs are able to diffuse long distances in a given time and fuse with targeted cells[12]. The combination of these features allows EVs to serve as natural delivery vehicles[58]. One of the key features of EVs is that they have a large surface compared to volume[59]. Therefore, surface properties or molecular interactions at the surface of EVs may perform important functions. In this study, we found that TfR, CD163 and CD91 are integrated on the EV surface, which ensures the iron recycling capacity of EVs through capture of the iron-containing molecules to facilitate iron recycling. These 'iron catchers' enhance the efficiency of iron sequestration and resistance to bacterial infection, thereby highlighting a previously unknown mechanism of innate immunity. The results of this study suggest that infusing TfR-, CD163- and CD91-bearing EVs provides a potential strategy for combating bacterial infection. Although herein we focus on small EVs, it is also important to evaluate the role of other kinds of EVs, including microvesicles or apoptotic bodies, in iron metabolism and infection defense because bacterial infection may also regulate the release of EVs[51]. In this study, we mainly focused on EVs derived from macrophages. In fact, circulating EVs of other origin may also participate in iron metabolism regulation via membrane receptors. Additionally, whether EVs in circulation regulate other kinds of nutrients or small molecules still needs to be determined and future studies may provide more evidence for extracellular vesicle-based metabolism regulation. It has been reported that

there was no significant difference in the incidence of *Salmonella* infection between men and women[60,61]; however, the mechanism revealed in this study may still differ between male and female mice. The use of only female mice is a limitation of this study. Further studies are needed to demonstrate the mechanism in male mice.

Methods

Bacterial strains and growth conditions
S. Typhimurium (ATCC14028) and *S. aureus* (ATCC6538) were purchased from Beijing Beina Biological. *S*. Typhimurium and *S. aureus* were grown overnight in Luria-Bertani (LB) broth (10 g tryptone, 5 g yeast extract and 10 g NaCl l^{-1}) at 37 °C with shaking. Bacterial density was confirmed by dilution plating. To obtain HK *S*. Typhimurium, *S*. Typhimurium were cultured in LB broth overnight at 37 °C, centrifuged in 4,000*g* for 5 min and resuspended in PBS. The resuspended bacteria were boiled at 70 °C for 1 h before being used immediately.

Cell culture
BMDMs were obtained by collecting bone marrow from femurs and tibias of C57BL/6J wild-type mice. Bone marrow cells were flushed out with PBS and lysed with red blood cell lysis buffer (Beyotime). After centrifugation for 5 min at 800*g*, cells were seeded in plates and incubated with Dulbecco's modified Eagle's medium (DMEM) containing 10% fetal bovine serum (FBS) and 20 ng ml^{-1} macrophage colony-stimulating factor (M-CSF) (PeproTech). Mature BMDMs were used for the next experiments until 7–8 d. Mature BMDMs were infected with *S*. Typhimurium at an m.o.i. (bacteria per macrophage) of 10. Cells were incubated in DMEM without FBS and antibiotics. After incubating for 30 min, cells were washed with PBS and replaced with fresh DMEM containing 10% EV-depleted FBS. Mock-infected wells received an equivalent volume of PBS. For *S. aureus* infection, BMDMs were infected with *S. aureus* at an m.o.i. of 25 for 1 h. Subsequently, extracellular bacteria were removed by washing with PBS. BMDMs were cultured in fresh DMEM containing 10% EV-depleted FBS. When indicated, infected BMDMs were treated with 5 mM 4-PBA (MedChemExpress) or 0.5 μM Torin-1 (MedChemExpress). Mature BMDM were treated with 100 nM bafilomycin A1 (MedChemExpress) as the positive control of lysosomal dysfunction.

siRNA and transfection
BMDMs were transfected with siRNA (RiBOBIO) targeting Rab31 and IRE1α mRNAs using Advanced DNA RNA Transfection Reagent (Zeta Life) according to the manufacturer's instructions. Subsequent treatments on transfected cells were performed 24 h after transfection. BMDMs were infected with lentivirus containing Rab27a shRNA expression vector (Shanghai Jikai Gene) according to the manufacturer's instructions.

Preparation and characterization of liposome-encapsulated 4-PBA
According to the procedure previously described by Chen et al.[62]. Liposome-encapsulated 4-PBA was prepared with hydrogenated soybean phosphatidylcholine (Sinopharm) and cholesterol (Sinopharm) by the ethanol injection method. Subsequently, to estimate the encapsulation efficiency for liposome-encapsulated 4-PBA, 4-PBA was labeled with RhB and the content of 4-PBA was analyzed by fluorescence spectrometry (PerkinElmer).

Animal experiment
All animal experiments were approved by the Animal Care Committee of the Fourth Military Medical University. Wild-type 6–8-week-old female C57BL/6J mice were obtained from the Laboratory Animal Research Center of the Fourth Military Medical University. All mice were housed in a 12-h dark–light cycle at 22 ± 2 °C and 40% humidity. All mice were allowed access to a standard diet containing approximately 180 mg iron per kg chow, which was obtained from Jiangsu Province

Collaborative Medical Bioengineering. To identify the function of EVs in *S.* Typhimurium infection, mice were preinjected intraperitoneally (i.p.) with GW4869 (MedChemExpress) at a dose of $1.5\,\mu g\,g^{-1}$ for 6 h, followed by an i.p. injection of 3×10^5 c.f.u. of *S.* Typhimurium. GW4869 was initially dissolved in dimethylsulfoxide into a stock solution of $10\,mg\,ml^{-1}$. The working solution was further diluted in PBS before use. To analyze early changes in serum iron, mice were killed 12 h after *S.* Typhimurium infection. Mice received injections of PBS as a control. The survival rate of the mice was monitored every 12 h for a period of 9 d. To further verify the effects of EV release on *S.* Typhimurium infection, mice that received GW4869 and *S.* Typhimurium were i.v. injected with EVs (100 μg) 1 h and 6 h after *S.* Typhimurium infection. The EVs used for the experiments were isolated from the supernatant of uninfected or infected BMDMs or from the serum of uninfected or infected mice. Mice were killed at 24 h after infection. The survival rate of the mice was monitored every 12 h for 10 d.

Mice were i.p. treated with 3×10^7 c.f.u. of HK *S.* Typhimurium to induce endogenous EV release. In addition, mice were i.p. injected with iron-dextran ($50\,\mu g\,g^{-1}$ body weight, Sigma) to establish an iron-loaded mouse model. To verify the effect of ERS on EV release, mice were treated with 3×10^5 c.f.u. of *S.* Typhimurium. At 6 h after infection, mice were injected with ($10\,mg\,kg^{-1}$ body weight) liposome-encapsulated 4-PBA or an equivalent volume of empty liposomes. To test the changes in iron and EVs, blood and tissues were collected at 12 h after 4-PBA injection.

Depletion of macrophages and BMDM adoptive transfer assay
Liposome-encapsulated clodronate (200 μl per 20 g body weight; 40337ES08, YeaSen) or liposome-encapsulated PBS (40338ES05, YeaSen) was i.v. injected to deplete macrophages in mice as described previously[63]. The depletion efficiency was measured by flow cytometry analysis. Two days after liposome-encapsulated treatment, macrophage-depleted mice were i.v. injected with BMDMs (2×10^6 cells per mouse).

Flow cytometric analysis
BMDMs were incubated with PE-conjugated anti-mouse F4/80 antibodies (123110, BioLegend) and FITC-conjugated anti-mouse CD11b antibodies (101206, BioLegend) at 4 °C for 1 h. Mouse spleen was homogenized, filtered through a cell strainer and subjected to red cell lysis buffer (Beyotime). The cell suspension was then incubated with PE-conjugated anti-mouse MHC II antibodies (116407, BioLegend) and Alexa Fluor 488 anti-mouse F4/80 antibodies (123120, BioLegend) at 4 °C for 1 h. After incubation, the cells were analyzed with a CytoFLEX flow cytometer (Beckman Coulter). Data were analyzed with FlowJo software (FlowJo). For in vitro BMDM characterization, FSC-SSC-H gating was used as a preliminary gating followed by CD11b⁺ or F4/80⁺ population. For the proportion of macrophages in the spleen, FSC-SSC-H gating was used as preliminary gating followed by double-positive MHCII⁺/F4/80⁺ population.

The determination of bacteria burden in blood and tissues
The blood was collected in a tube with heparin sodium to prevent blood from coagulation. The mouse liver or spleen was aseptically excised, weighed and homogenized in PBS. Bacteria c.f.u. were counted by plating dilutions of blood or suspension of homogenized liver or spleen on LB plates after incubation at 37 °C.

Serum and tissue iron measurements
Blood was collected into EP tubes and allowed to clot at 4 °C for 12 h followed by centrifugation at 1,550*g* for 10 min. The serum was used for analysis of iron levels. For liver and spleen iron measurements, the tissue was mixed with iron assay buffer. After homogenization, the mixture was centrifuged at 16,000*g* for 10 min at 4 °C and the supernatant was used for the iron assay. Total iron was detected using an

Iron Assay kit according to the manufacturer's instructions (Abcam). In brief, 1–50 μl serum or other liquid samples were added to a 96-well plate and the volume was brought to 100 μl per well with assay buffer. Iron reducer was then added to each of the sample wells and incubated in the dark for 30 min at 37 °C. After the first incubation, 100 μl of iron probe was added to each well and incubated in the dark for 60 min at 37 °C. Absorbance was measured at 593 nm using microplate reader (Bio-Rad).

Histopathological evaluation
The liver and spleen samples were placed in 4% paraformaldehyde (PFA) overnight at 4 °C, embedded in paraffin blocks, sliced into 4-μm thick sections and stained with H&E. After staining, sections were evaluated with a Leica DM4B Microscope (Leica). The degree of liver injury was determined by histological scoring analysis. The assessment was expressed as the sum of the individual score grades of 0 (normal), 1 (mild injury), 2 (moderate injury), 3 (severe injury) and 4 (maximum injury) for each of the following five categories: inflammation infiltration, cytoplasm vacuolization, nuclear condensation, hemorrhage and hepatocyte necrosis. To evaluate the splenic histological changes, a semiquantitative scoring system was used. The histopathological changes in the spleen were classified based on the severity of three histological criteria: architecture loss, necrotic cells and inflammation. The histopathological changes were graded on a scale as follows: absent (0), slight (1), moderate (2) and pronounced (3).

Immunofluorescence staining
For tissues, the liver or spleen was fixed in 4% PFA for 24 h. After washing with PBS, the samples were immersed in 30% sucrose solution for 24 h and then embedded in optimum cutting temperature compound (Tissue OCT-Freeze Medium). The tissues were prepared as 10-μm sections. After permeation with 0.1% Triton X-100 (Sigma), cryosections were blocked with goat serum (Boster) for 1 h at room temperature. Then, cryosections were incubated with the following antibodies: anti-F4/80 antibody (1:200 dilution, ab6640, Abcam), anti-GRP78/Bip antibody (1:200 dilution, ab21685, Abcam), anti-macrophage antibody (1:200 dilution, ab22506, Abcam) and anti-*S.* Typhimurium LPS antibody (1:200 dilution, ab8274, Abcam) at 4 °C overnight. After washing with PBS, sections were incubated with Alexa Fluor 488/594-conjugated secondary antibodies (1:200 dilution, YeaSen) at 37 °C for 1 h, followed by staining with Hoechst 33342 for 10 min. Finally, immunofluorescence images were obtained by confocal laser scanning microscopy (CLSM) (Nikon).

For cells, BMDMs were grown in 24-well plates containing coverslips before the indicated treatments. After treatment, cells were washed with PBS, fixed with 4% PFA for 30 min and blocked with 5% BSA for 1 h at room temperature. Cells were then incubated with anti-F4/80 antibody (1:200 dilution) or anti-GRP78/Bip antibody (1:200 dilution) or anti-LAMP1 antibody (1:200 dilution, ab24170, Abcam) overnight at 4 °C followed by incubation with secondary antibody. The cells were stained with Hoechst and visualized by CLSM. To analyze ROS levels in cells, a Reactive Oxygen Species Assay kit (50101ES01, YeaSen) was used. Cells were collected at the indicated time points and washed with PBS. Then, cells were incubated with DCFH-DA at a final concentration of 10 μM at 37 °C for 30 min in the dark. After washing with PBS, cells were fixed with 4% PFA for 30 min at 4 °C. Finally, cells were stained with Hoechst and visualized by CLSM.

Intracellular Ca²⁺ measurement
To analyze the intracellular Ca^{2+} levels in cells, BMDMs were loaded with the cell permeant Ca^{2+} indicator Fluo-4, AM (40704ES50, YeaSen) in calcium-free Hank's balanced salt solution at a final concentration of 5 μM for 30 min (37 °C). The green fluorescence of Ca^{2+} was measured with a multimode plate reader (PerkinElmer) and CLSM (Nikon).

LysoTracker and Magic Red fluorescence measurement

To measure lysosomal acidity, cells were incubated in serum-free medium with 50 nM LysoTracker (40739ES50, YeaSen) and 1 µM Magic Red (ab70774, Abcam) at 37 °C for 30 min. After washing with PBS, LysoTracker fluorescence intensity was measured with a multimode plate reader (PerkinElmer) and CLSM (Nikon). Magic Red fluorescence intensity was measured by CLSM (Nikon).

EV isolation and characterization

Cell supernatant or serum was centrifuged at $800g$ for 5 min to remove cells or cell debris. The supernatant was then centrifuged at $16,000g$ for 30 min to remove microvesicles. Then, the supernatant was ultracentrifuged at 4 °C for 70 min at $150,000g$, followed by washing with PBS and purification by ultracentrifugation at $150,000g$ for 70 min. EVs were collected from the bottom of the tube. The concentration was measured by a BCA kit (Beyotime) or NanoSight NS300 (Malvern). For NanoSight tracking analysis, EVs were diluted to obtain 10–100 particles per image. The size of EVs was examined using NTA with Zeta View PMX 110 (Particle Metrix) and corresponding software Zeta View v.8.04.02.

Electron microscopy

For TEM, a drop of suspension containing EVs was applied to a 200-mesh carbon-stabilized copper grids. EVs were allowed to absorb for 5 min before the excess suspension was wicked off. Next, the grid was stained with 2% phosphotungstic acid hydrate for 30 s followed by washing with distilled water three times. Excess solution was wicked off and the grid was allowed to air-dry before observation. For immunogold staining, EVs were mixed with an equal volume of 2.54% glutaraldehyde for 20 min at room temperature and then applied to 200-mesh nickel grids. After blocking with 5% BSA, the grid was incubated with a 1:20 dilution of the primary antibody (anti-CD163 antibody, anti-CD91 antibody and anti-TfR antibody) for 1 h at room temperature. After washing with ultrapure water, the grid was treated with 10-nm gold-labeled secondary antibody (Electron Microscopy Sciences) for 30 min. The grid was then washed with ultrapure water and stained with 2% phosphotungstic acid hydrate for 30 s, followed by rinsing with ultrapure water. After dying, all grids were examined by TEM (TECNAI Spirit, FEI).

In vitro and in vivo fluorescence tracing of EVs and liposome-encapsulated 4-PBA

For in vitro tracing of liposome-encapsulated 4-PBA in macrophages, BMDMs were treated with RhB-labeled liposome-encapsulated 4-PBA for 3 h. Cells were then washed with PBS and fixed with 4% PFA for 30 min at room temperature. Cells were blocked with 5% BSA, incubated with F4/80 antibody at 4 °C overnight and treated with Alexa Fluor 488-conjugated secondary antibodies. Cell nuclei were counterstained with Hoechst 33342. At the end of the experiment, cells were washed with PBS and observed using CLSM. For ex vivo fluorescence tracing of EVs and liposome-encapsulated 4-PBA, DiR-labeled EVs or RhB-labeled liposome-encapsulated 4-PBA were administered into mice via i.v. or i.p. injection, respectively. After 24 h, mice were killed and organs were collected and subjected to ex vivo bioluminescence imaging performed by an In Vivo Imaging System (Xenogen). The luminescent signal was evaluated manually using Living Image Software (Calliper LifeSciences). To verify the specific uptake of EVs by S. Typhimurium, S. Typhimurium expressing mCherry (S. Typhimurium–mCherry) were treated with PKH-67-labeled EVs for 3 h. Then, the bacterial suspension containing EVs was smeared thinly on a glass slide and observed by CLSM.

Iron-binding assay

The GW4869-pretreated infected mouse serum was collected and serum EVs were removed by ultracentrifugation at $150,000g$ for 70 min at 4 °C. Then different EVs were added to the serum. To block transferrin binding to TfR, EVs were preincubated with excess amount of holo-transferrin (Sigma). After incubation the added EVs were isolated by ultracentrifugation at $150,000g$ for 70 min at 4 °C. The serum supernatant and the EV fraction were collected. The total iron levels in the supernatant were measured by Iron Assay kit (Abcam). The transferrin levels in the supernatant were analyzed by ELISA (Elabscience). In addition, the serum supernatant was heated at 56 °C for 1 h and S. Typhimurium or S. aureus were inoculated into the supernatant. The cultures were then maintained under continuous shaking at 37 °C with optical measurements at OD_{490} or OD_{620} every 12 h.

Quantification of transferrin in serum and EVs

To expose the transferrin protein in the EV fraction, the EV fraction was suspended in 1% Triton X-100 for 30 min at room temperature. After centrifugation at $12,000g$ for 10 min, EV lysates were collected. The levels of transferrin were measured in serum and EV lysates using an ELISA kit (Elabscience) according to the manufacturer's instructions.

Western blot

Samples were lysed on ice in lysis buffer (Beyotime) containing a protease inhibitor for 30 min. Protein samples (20 µg) quantified by BCA assay were loaded on an 8–12% SDS–polyacrylamide gel and then transferred to PVDF membranes (Merck Millipore) for 2 h. The membrane was blocked with 5% BSA at room temperature for 1 h and then incubated with primary antibody overnight at 4 °C. The membranes were then incubated with HRP-labeled secondary antibody for 1 h at room temperature and was processed by chemiluminescent kit (Merck Millipore) with an imaging system (Tanon 4600). The anti-CD81 antibody (ab109201), anti-TSG101 antibody (ab125011), anti-calnexin antibody (ab22595), anti-TfR antibody (ab84036), anti-CD91 antibody (ab92544), anti-CD163 antibody (ab182422), anti-ATF6 antibody (ab203119), anti-ATP6V1A antibody (ab199326), anti-GRP78 antibody (ab21658), anti-LAMP1 antibody (ab24170), anti-ATP6V1B antibody (ab200839) and anti-Rab31 antibody (ab230881) were purchased from Abcam. The anti-CD63 antibody (sc-5275) was obtained from Santa Cruz. The anti-Alix antibody (92880), anti-ATF4 antibody (11815), anti-IRE1α antibody (3294), anti-TFEB antibody (32361), anti-Erk1/2 antibody (9102s), anti-phospho-Erk1/2 antibody (9101s) and anti-FTH1 antibody (3998S) were purchased from Cell Signaling Technology. The anti-FPN1 antibody (PA5-115915) was purchased from Invitrogen. The anti-GAPDH antibody was obtained from YeaSen. The secondary antibodies (peroxidase AffiniPure goat anti-mouse immunoglobulin G (IgG), DY60203; peroxidase AffiniPure goat anti-rabbit IgG, DY60202) were all purchased from DIYIBio.

Data presentation and statistical analysis

Data are presented as mean ± s.d and were analyzed using SPSS v.19.0 software. For all tests, differences of $P < 0.05$ were considered indicative of significance. Survival curves were compared using the log-rank test. Data normality and equal variances were assessed before comparisons. For normally distributed data with equal variances, pairwise comparisons were made using unpaired two-tailed Student's *t*-tests and multiple samples were compared using one-way ANOVA with Tukey's correction. Other data were compared using the Mann–Whitney *U*-test or Kruskal–Wallis test. The number of independent experiments and relevant statistical methods for each panel are detailed in the figure legends. No statistical methods were used to predetermine sample sizes but our sample sizes are similar to those reported in previous publications[17,64–66]. No animals or data points were excluded.

Reporting summary

Further information on research design is available in the Nature Portfolio Reporting Summary linked to this article.

Data availability

All the data supporting the findings of this study are available within this article and the Supplementary Information files. Other information of this study is available from the corresponding author upon reasonable request. Source data are provided with this paper.

References

1. Thornton, F. J., Schäffer, M. R. & Barbul, A. Wound healing in sepsis and trauma. *Shock* **8**, 391–401 (1997).

2. Cassat, J. E. & Skaar, E. P. Iron in infection and immunity. *Cell Host Microbe* **13**, 509–519 (2013).

3. Wang, J. & Pantopoulos, K. Regulation of cellular iron metabolism. *Biochem. J.* **434**, 365–381 (2011).

4. Soares, M. P. & Hamza, I. Macrophages and iron metabolism. *Immunity* **44**, 492–504 (2016).

5. Kalluri, R. The biology and function of exosomes in cancer. *J. Clin. Invest.* **126**, 1208–1215 (2016).

6. Brahmer, A. et al. Platelets, endothelial cells and leukocytes contribute to the exercise-triggered release of extracellular vesicles into the circulation. *J. Extracell. Vesicles* **8**, 1615820 (2019).

7. Bhatnagar, S. & Schorey, J. S. Exosomes released from infected macrophages contain *Mycobacterium avium* glycopeptidolipids and are proinflammatory. *J. Biol. Chem.* **282**, 25779–25789 (2007).

8. Bhatnagar, S., Shinagawa, K., Castellino, F. J. & Schorey, J. S. Exosomes released from macrophages infected with intracellular pathogens stimulate a proinflammatory response in vitro and in vivo. *Blood* **110**, 3234–3244 (2007).

9. Verweij, F. J. et al. Live tracking of inter-organ communication by endogenous exosomes in vivo. *Dev. Cell* **48**, 573–589 (2019).

10. Villarroya-Beltri, C. et al. ISGylation controls exosome secretion by promoting lysosomal degradation of MVB proteins. *Nat. Commun.* **7**, 13588 (2016).

11. Jeppesen, D. K. et al. Reassessment of exosome composition. *Cell* **177**, 428–445 (2019).

12. Kastelowitz, N. & Yin, H. Exosomes and microvesicles: identification and targeting by particle size and lipid chemical probes. *ChemBioChem* **15**, 923–928 (2014).

13. Keller, M. D. et al. Decoy exosomes provide protection against bacterial toxins. *Nature* **579**, 260–264 (2020).

14. Drakesmith, H. & Prentice, A. M. Hepcidin and the iron-infection axis. *Science* **338**, 768–772 (2012).

15. Shutinoski, B. et al. Lrrk2 alleles modulate inflammation during microbial infection of mice in a sex-dependent manner. *Sci. Transl. Med.* **11**, eaas9292 (2019).

16. Wang, L. et al. Selective modulation of TLR4-activated inflammatory responses by altered iron homeostasis in mice. *J. Clin. Invest.* **119**, 3322–3328 (2009).

17. Kim, D. K. et al. Inverse agonist of estrogen-related receptor γ controls *Salmonella* Typhimurium infection by modulating host iron homeostasis. *Nat. Med.* **20**, 419–424 (2014).

18. Essandoh, K. et al. Blockade of exosome generation with GW4869 dampens the sepsis-induced inflammation and cardiac dysfunction. *Biochim. Biophys. Acta* **1852**, 2362–2371 (2015).

19. Iguchi, Y. et al. Exosome secretion is a key pathway for clearance of pathological TDP-43. *Brain* **139**, 3187–3201 (2016).

20. Walker, J. et al. Lipoxin a4 increases survival by decreasing systemic inflammation and bacterial load in sepsis. *Shock* **36**, 410–416 (2011).

21. Gan, Z. et al. Regulation of macrophage iron homeostasis is associated with the localization of bacteria. *Metallomics* **11**, 454–461 (2019).

22. Kapetanovic, R. et al. Pig bone marrow-derived macrophages resemble human macrophages in their response to bacterial lipopolysaccharide. *J. Immunol.* **188**, 3382–3394 (2012).

23. Winn, N. C., Volk, K. M. & Hasty, A. H. Regulation of tissue iron homeostasis: the macrophage "ferrostat". *JCI Insight* https://doi.org/10.1172/jci.insight.132964 (2020).

24. Mayhew, T. M. & Lucocq, J. M. Developments in cell biology for quantitative immunoelectron microscopy based on thin sections: a review. *Histochem Cell Biol.* **130**, 299–313 (2008).

25. Ratledge, C. & Dover, L. G. Iron metabolism in pathogenic bacteria. *Annu. Rev. Microbiol.* **54**, 881–941 (2000).

26. Nairz, M., Schroll, A., Sonnweber, T. & Weiss, G. The struggle for iron: a metal at the host–pathogen interface. *Cell Microbiol.* **12**, 1691–1702 (2010).

27. Otto, B. R., Verweij-van Vught, A. M. & MacLaren, D. M. Transferrins and heme-compounds as iron sources for pathogenic bacteria. *Crit. Rev. Microbiol.* **18**, 217–233 (1992).

28. Dichtl, S. et al. Dopamine is a siderophore-like iron chelator that promotes *Salmonella enterica* serovar Typhimurium virulence in mice. *mBio* https://doi.org/10.1128/mbio.02624-18 (2019).

29. Haley, K. P. & Skaar, E. P. A battle for iron: host sequestration and *Staphylococcus aureus* acquisition. *Microbes Infect.* **14**, 217–227 (2012).

30. Lokken, K. L., Tsolis, R. M. & Bäumler, A. J. Hypoferremia of infection: a double-edged sword? *Nat. Med.* **20**, 335–337 (2014).

31. Arezes, J. et al. Hepcidin-induced hypoferremia is a critical host defense mechanism against the siderophilic bacterium *Vibrio vulnificus*. *Cell Host Microbe* **17**, 47–57 (2015).

32. Ganz, T. Iron in innate immunity: starve the invaders. *Curr. Opin. Immunol.* **21**, 63–67 (2009).

33. Liao, Z. et al. Heat-killed *Salmonella* Typhimurium protects mice against carbon ion radiation. *J. Int Med Res* **48**, 300060520924256 (2020).

34. Abels, E. R. & Breakefield, X. O. Introduction to extracellular vesicles: biogenesis, RNA cargo selection, content, release, and uptake. *Cell Mol. Neurobiol.* **36**, 301–312 (2016).

35. Rashid, H. O., Yadav, R. K., Kim, H. R. & Chae, H. J. ER stress: autophagy induction, inhibition and selection. *Autophagy* **11**, 1956–1977 (2015).

36. Moretti, J. et al. STING senses microbial viability to orchestrate stress-mediated autophagy of the endoplasmic reticulum. *Cell* **171**, 809–823 (2017).

37. Zhang, Y. et al. Hepatotoxicity induced by isoniazid-lipopolysaccharide through endoplasmic reticulum stress, autophagy, and apoptosis pathways in zebrafish. *Antimicrob. Agents Chemother.* https://doi.org/10.1128/aac.01639-18 (2019).

38. Settembre, C. et al. TFEB links autophagy to lysosomal biogenesis. *Science* **332**, 1429–1433 (2011).

39. Nguyên, D. T. et al. Nck-dependent activation of extracellular signal-regulated kinase-1 and regulation of cell survival during endoplasmic reticulum stress. *Mol. Biol. Cell* **15**, 4248–4260 (2004).

40. Martina, J. A., Chen, Y., Gucek, M. & Puertollano, R. MTORC1 functions as a transcriptional regulator of autophagy by preventing nuclear transport of TFEB. *Autophagy* **8**, 903–914 (2012).

41. Roczniak-Ferguson, A. et al. The transcription factor TFEB links mTORC1 signaling to transcriptional control of lysosome homeostasis. *Sci. Signal* **5**, ra42 (2012).

42. Hua, S. & Wu, S. Y. The use of lipid-based nanocarriers for targeted pain therapies. *Front. Pharm.* **4**, 14 (2013).

43. Caza, M. & Kronstad, J. W. Shared and distinct mechanisms of iron acquisition by bacterial and fungal pathogens of humans. *Front. Cell Infect. Microbiol.* **3**, 80 (2013).

44. Patruta, S. I. & Hörl, W. H. Iron and infection. *Kidney Int. Suppl.* **69**, S125–S130 (1999).

45. Sarwar, H. S. et al. Redox biology of *Leishmania* and macrophage targeted nanoparticles for therapy. *Nanomedicine* **12**, 1713–1725 (2017).

46. Wandersman, C. & Delepelaire, P. Bacterial iron sources: from siderophores to hemophores. *Annu. Rev. Microbiol.* **58**, 611–647 (2004).

47. Hood, M. I. & Skaar, E. P. Nutritional immunity: transition metals at the pathogen-host interface. *Nat. Rev. Microbiol.* **10**, 525–537 (2012).

48. Xiao, X., Yeoh, B. S. & Vijay-Kumar, M. Lipocalin 2: an emerging player in iron homeostasis and inflammation. *Annu. Rev. Nutr.* **37**, 103–130 (2017).

49. Lin, J. et al. A *Pseudomonas* T6SS effector recruits PQS-containing outer membrane vesicles for iron acquisition. *Nat. Commun.* **8**, 14888 (2017).

50. Carrière, J., Bretin, A., Darfeuille-Michaud, A., Barnich, N. & Nguyen, H. T. T. Exosomes released from cells infected with Crohn's disease–associated adherent-invasive *Escherichia coli* activate host innate immune responses and enhance bacterial intracellular replication. *Inflamm. Bowel Dis.* **22**, 516–528 (2016).

51. Schorey, J. S., Cheng, Y., Singh, P. P. & Smith, V. L. Exosomes and other extracellular vesicles in host–pathogen interactions. *EMBO Rep.* **16**, 24–43 (2015).

52. Catalano, M. & O'Driscoll, L. Inhibiting extracellular vesicles formation and release: a review of EV inhibitors. *J. Extracell. Vesicles* **9**, 1703244 (2020).

53. Zhao, Y. et al. Liver governs adipose remodelling via extracellular vesicles in response to lipid overload. *Nat. Commun.* **11**, 1–17 (2020).

54. Huang, Y. et al. Zika virus propagation and release in human fetal astrocytes can be suppressed by neutral sphingomyelinase-2 inhibitor GW4869. *Cell Discov.* **4**, 1–16 (2018).

55. Chiou, N. T., Kageyama, R. & Ansel, K. M. Selective export into extracellular vesicles and function of tRNA fragments during T cell activation. *Cell Rep.* **25**, 3356–3370 (2018).

56. Jeong, M. H., Kim, H. R., Park, Y. J., Chung, K. H. & Kim, H. S. Reprogrammed lung epithelial cells by decrease of miR-451a in extracellular vesicles contribute to aggravation of pulmonary fibrosis. *Cell Biol. Toxicol.* **38**, 725–740 (2022).

57. Kalluri, R. & LeBleu, V. S. The biology, function, and biomedical applications of exosomes. *Science* https://doi.org/10.1126/science.aau6977 (2020).

58. Wortzel, I., Dror, S., Kenific, C. M. & Lyden, D. Exosome-mediated metastasis: communication from a distance. *Dev. Cell* **49**, 347–360 (2019).

59. Buzás, E. I., Tóth, E., Sódar, B. W. & Szabó-Taylor, K. Molecular interactions at the surface of extracellular vesicles. *Semin. Immunopathol.* **40**, 453–464 (2018).

60. Luo, L. et al. Epidemiological and clinical differences between sexes and pathogens in a three-year surveillance of acute infectious gastroenteritis in Shanghai. *Sci. Rep.* **9**, 1–9 (2019).

61. Stanaway, J. D. et al. The global burden of non-typhoidal Salmonella invasive disease: a systematic analysis for the Global Burden of Disease Study 2017. *Lancet Infect. Dis.* **19**, 1312–1324 (2019).

62. Chen, Y. Q. et al. Delivery of rapamycin by liposomes synergistically enhances the chemotherapy effect of 5-fluorouracil on colorectal cancer. *Int J. Nanomed.* **16**, 269–281 (2021).

63. Nguyen, T., Du, J. & Li, Y. C. A protocol for macrophage depletion and reconstitution in a mouse model of sepsis. *STAR Protoc.* **2**, 101004–101017 (2021).

64. Flo, T. H. et al. Lipocalin 2 mediates an innate immune response to bacterial infection by sequestrating iron. *Nature* **432**, 917–921 (2004).

65. Liu, S. et al. Treatment of infarcted heart tissue via the capture and local delivery of circulating exosomes through antibody-conjugated magnetic nanoparticles. *Nat. Biomed. Eng.* **4**, 1063–1075 (2020).

66. Dou, G. et al. Chimeric apoptotic bodies functionalized with natural membrane and modular delivery system for inflammation modulation. *Sci. Adv.* **6**, eaba2987 (2020).

Acknowledgements

Author contributions

H.K. and G.D. designed, performed and interpreted the experiments and wrote the manuscript. L.C. and X.W. performed bacterial experiments and characterized properties of liposome. H.X., X.L., F.D. and Y.L. assisted with animal experiments. X.Y. and Siying Liu performed the histopathological studies and collected data. L.B., H.L. and B.L. contributed to data analysis and interpretation. Shiyu Liu developed the original concept. Shiyu Liu and Y.J. conceived the study and supervised the experiments.

Competing interests

The authors declare no competing interests.

Additional information

Extended data is available for this paper at https://doi.org/10.1038/s42255-022-00723-5.

Supplementary information The online version contains supplementary material available at https://doi.org/10.1038/s42255-022-00723-5.

**Correspondence and requests for materials** should be addressed to Yan Jin or Shiyu Liu.

Peer review information *Nature Metabolism* thanks Frederik Verweij, Günter Weiss and the other, anonymous, reviewer(s) for their contribution to the peer review of this work. Primary Handling Editor: Yanina-Yasmin Pesch, in collaboration with the *Nature Metabolism* team.

Reprints and permissions information is available at www.nature.com/reprints.
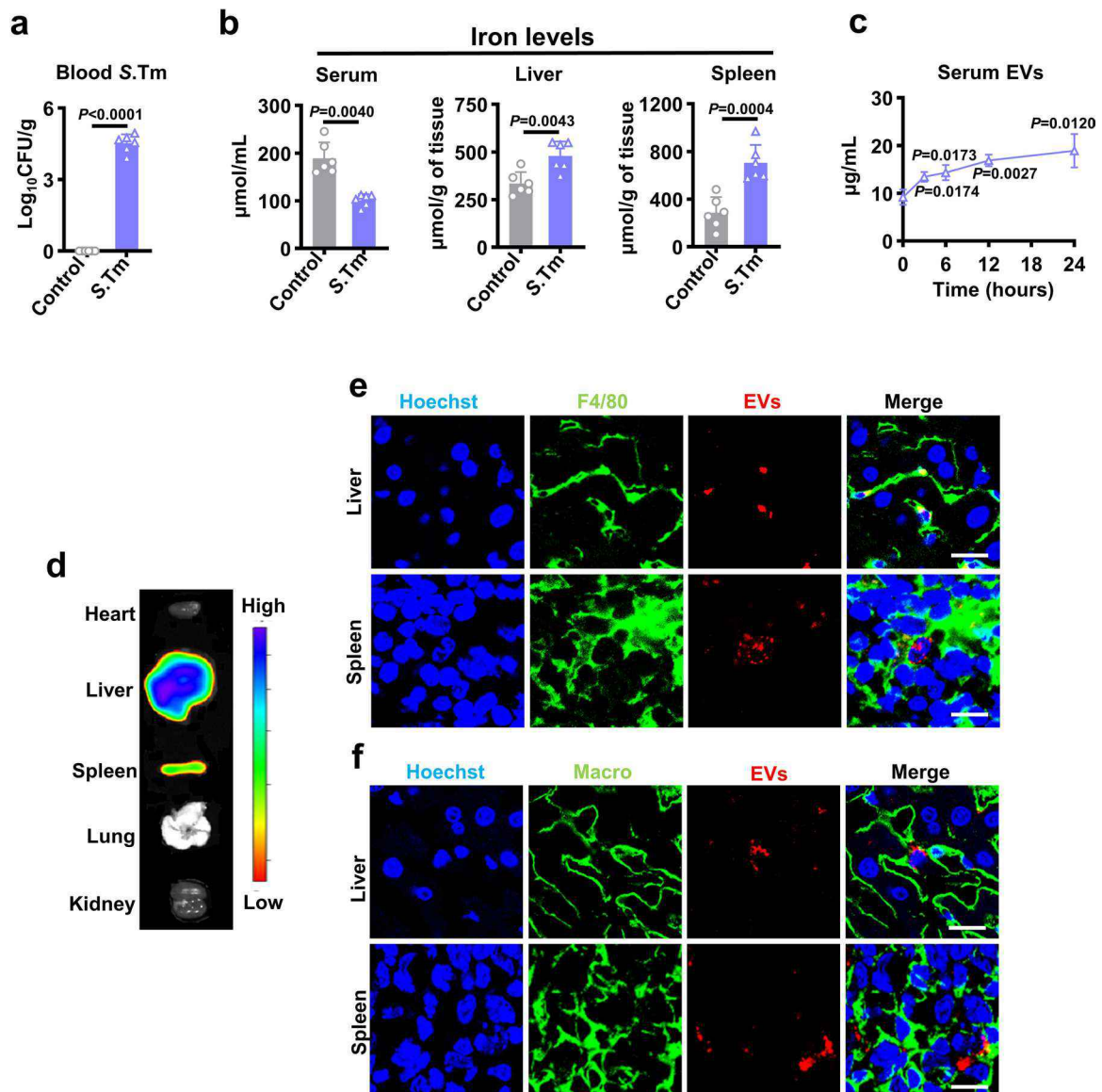
Extended Data Fig. 1 | The characterization of *S*.Tm-infected mice and serum EVs biodistribution *in vivo*. a-c, The C57BL/6 J mice were intraperitoneally administrated with *S*.Tm and blood and tissues samples were collected for further analysis. a, The viable counts of *S*.Tm in the blood at 24 hours after infection. n = 6 mice. b, Serum (left), hepatic (middle), and splenic (right) iron levels in mice at 24 hours after infection. n = 6 mice. c, The concentration of EVs in serum within 24 hours after infection. n = 3 mice per time point. d, *Ex vivo* fluorescence images of various organs in mice systemically injected with DiR-labeled serum EVs. n = 3 mice. e, f, Confocal microscopy images showing the uptake of PKH26-labeled EVs (red) by F4/80⁺ cells (green) (e) or Macro⁺ cells (green) (f) in liver or spleen. Scale bar, 10 μm. n = 3 biologically independent samples. For a-c, data are presented as the mean ± s.d. For a-c, statistical significance was assessed by unpaired two-sided Student's t-test.
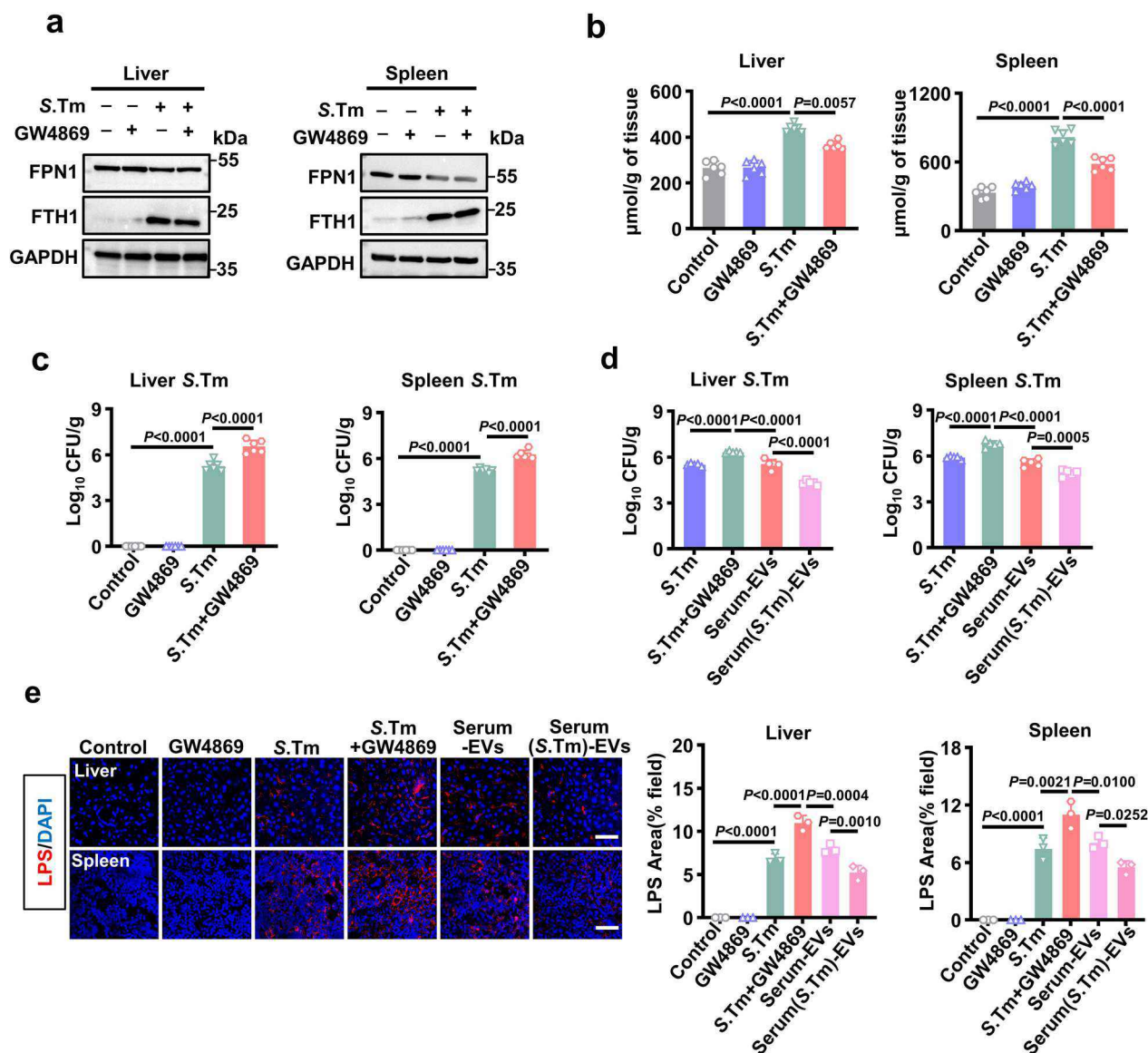
Extended Data Fig. 2 | The effect of EVs release blockade or EVs supplementation on the host defense response to S.Tm infection. a-c, To evaluate the effects of EVs release blockade on iron homeostasis, uninfected or S.Tm-infected mice were pretreated with GW4869 to block EVs release. a, Western blot analysis of FPN1 and FTH1 expressions in liver or spleen. Experiments were repeated three times and representative images are shown. **b**, The iron levels in liver or spleen at 12 hours after S.Tm infection. n = 6 mice. **c**, The viable count of S.Tm in liver and spleen at 12 hours after S.Tm infection. n = 6 mice. **d,e**, GW4869-pretreated S.Tm-infected mice were injected with EVs derived from uninfected mouse serum (Serum EVs group) or EVs derived from S.Tm-infected mouse serum [Serum(S.Tm)-EVs group]. **d**, The viable count of S.Tm in the liver and spleen. n = 5 mice. **e**, Representative fluorescence images of LPS (red) in the liver (upper) and spleen (bottom) and quantitative analysis of the percentage of LPS + area in liver or spleen cells. Scale bar, 50 μm. n = 3 biologically independent samples. For **b-e**, data are represented as the mean ± s.d. For **b-e**, statistical significance was assessed by one-way ANOVA with Tukey's post-hoc test.
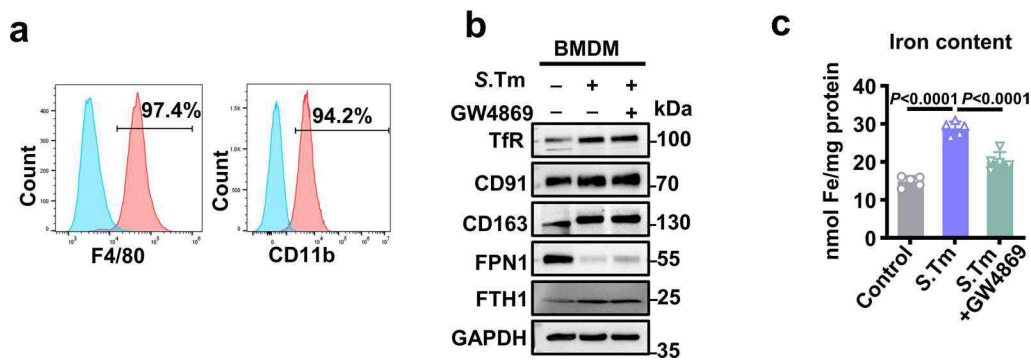
**Extended Data Fig. 3 | *S*.Tm infection affects iron homeostasis in BMDM.**
a, Flow cytometric analysis of the expressions of macrophage surface marker F4/80 and CD11b on BMDM. **b**, **c**, BMDM were treated with *S*.Tm in the absence or presence of GW4869 for 24 hours to determine the iron homeostasis. **b**, Western blot analysis of expressions of iron-related proteins TfR, CD91, CD163, FTH1, and FPN1. Experiments were repeated three times and representative images are shown. **c**, The iron content in BMDM. n = 5 biologically independent samples. For **c**, data are represented as the mean ± s.d. For **c**, statistical significance was assessed by one-way ANOVA with Tukey's post-hoc test.
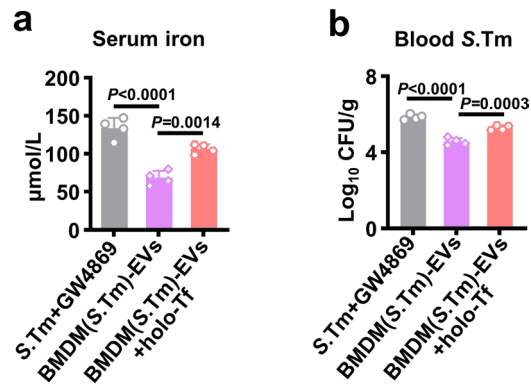
Extended Data Fig. 4 | EVs derived from *S*.Tm-infected BMDM decreased iron level and bacterial number in blood. a,b, The infected BMDM-derived EVs [BMDM(*S*.Tm)-EVs group] and infected BMDM-derived EVs pretreated with excess holo-transferrin [BMDM(*S*.Tm)-EVs+holo-Tf group] were injected into GW4869-pretreated infected mice respectively. **a**, The iron level in serum. n = 4 mice. **b**, Viable count of *S*.Tm in blood. n = 4 mice. For **a,b**, data are represented as the mean ± s.d. For **a,b**, statistical significance was assessed by one-way ANOVA with Tukey's post-hoc test.
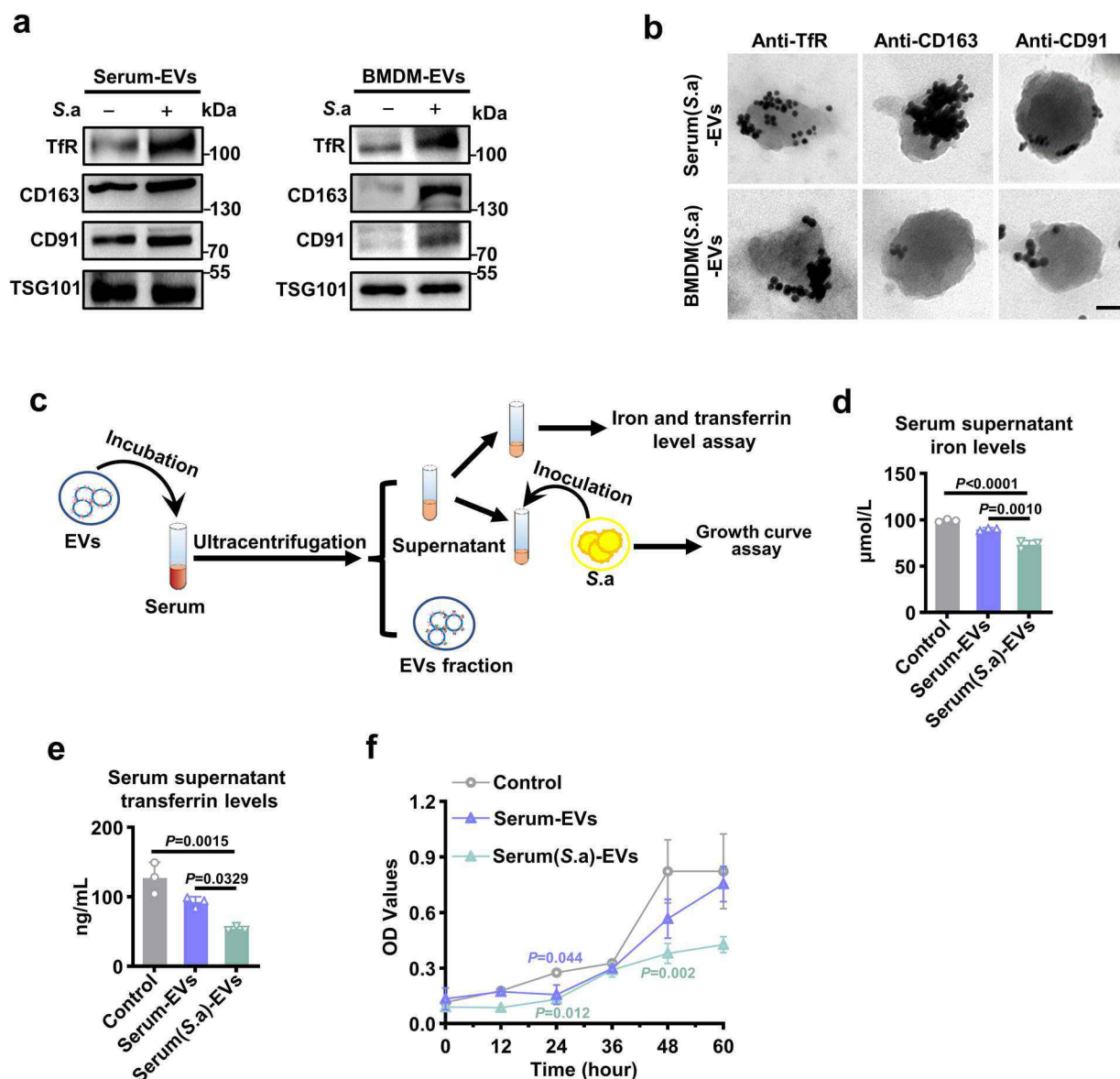
Extended Data Fig. 5 | TfR-, CD163-, CD91-bearing EVs derived from S.a-infected mice or BMDM bind iron. a-c, Wild-type mice was intraperitoneally injected with *S*.a and the serum were collected after 24 hours. BMDM were infected with *S*.a for 24 hours at a MOI of 25 and supernatant was collected. EVs were isolated from the serum or supernatant. **a**, Western blot analysis of TfR, CD163, CD91 and TSG101 expression in EVs derived from uninfected and infected mouse serum (left), and in EVs released from uninfected or infected BMDM (right). Experiments were repeated three times and representative images are shown. **b**, Immunoelectron microscopy detection for TfR, CD163, and CD91 antibodies in EVs derived from infected mouse serum (upper) or infected BMDM (bottom). Scale bar, 50 nm. Experiments were repeated twice and representative images are shown. **c**, Schematic diagram of the overall design of the experiments

to test the ability of EVs to bind iron in serum. EVs derived from uninfected mouse serum (Serum EVs group) or *S*.a-infected mouse serum [Serum (*S*.a)-EVs group] were added to the serum respectively and then removed by ultracentrifugation. The serum supernatant was collected for further analysis. **d, e**, Total iron levels (**d**) and transferrin levels (**e**) in the serum supernatant after incubation with EVs derived from uninfected or infected mouse serum. n = 3 biologically independent samples. **f**, Growth of *S*.a in serum supernatant. n = 5 biologically independent samples. For **d-f**, data are presented as the mean ± s.d. For **d** and **e**, statistical significance was assessed by one-way ANOVA with Tukey's post-hoc test. For **f**, statistical significance was assessed by one-way ANOVA with Tukey's post hoc test and Kruskal-Wallis test.

a

Serum EVs

b
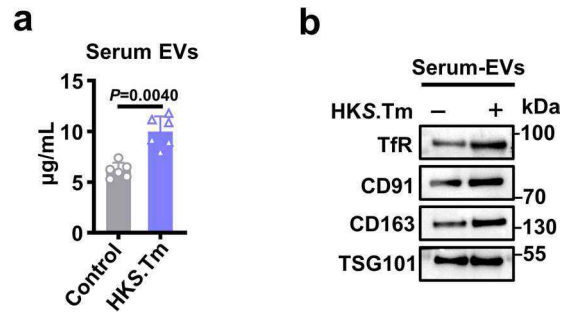
Serum-EVs

Extended Data Fig. 6 | HKS.Tm treatment enhances EVs release and expression of iron-related receptors. a, b, Wild-type mice were treated with HKS.Tm for 24 hours, and serum EVs were isolated. **a**, The concentration of EVs in serum. n = 6 mice. **b**, Western blot analysis of iron-related receptors TfR, CD91, and CD163 expressions on EVs. Experiments were repeated three times and representative images are shown. For **a**, data are presented as the mean ± s.d. For **a**, statistical significance was assessed by unpaired two-tailed Student's t-test.
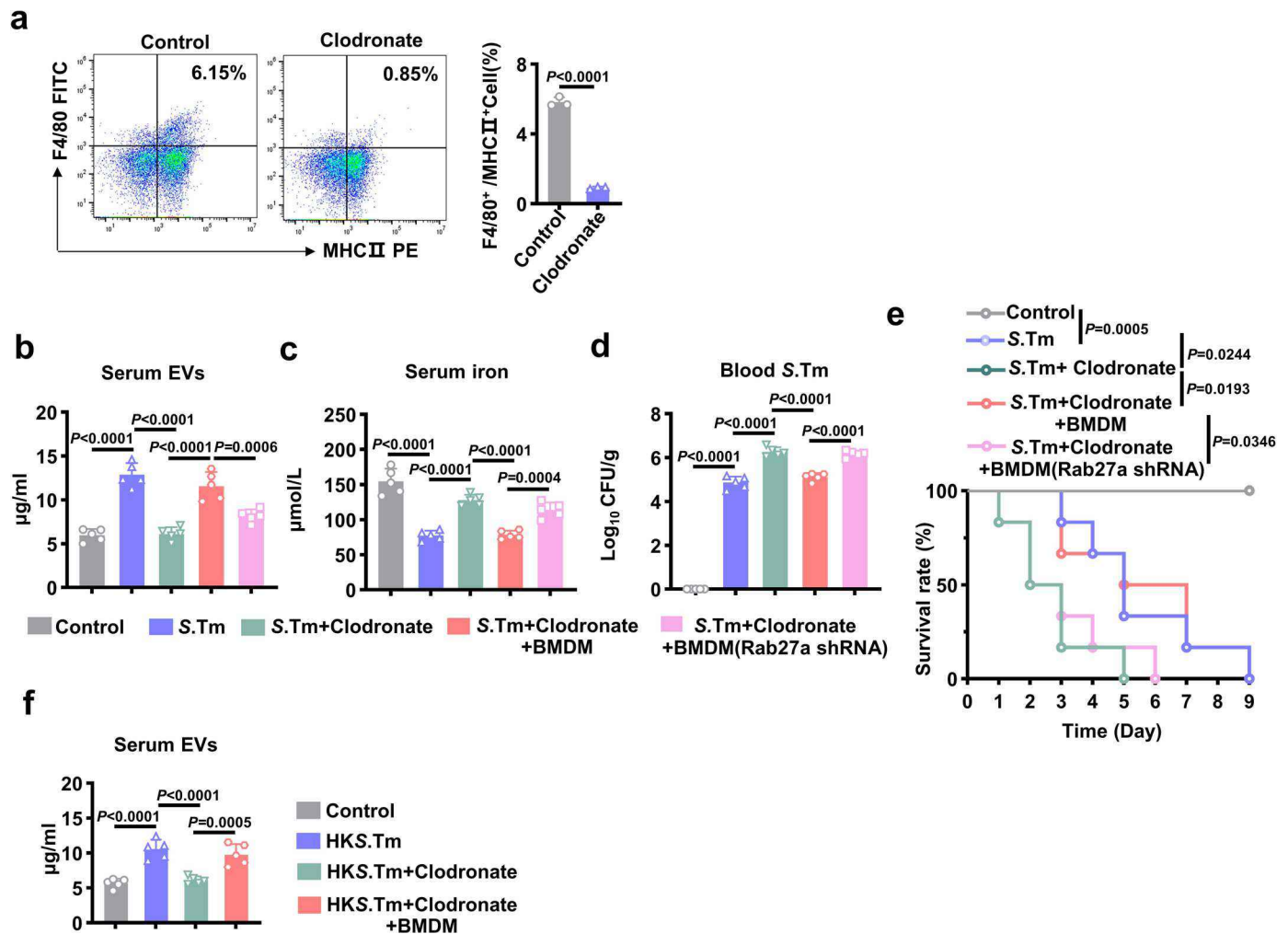
Extended Data Fig. 7 | EVs derived from macrophages protect against bacterial infection. a, Representative dot plots of mouse spleen macrophages analyses at 48 hours after treatment with liposome-encapsulated clodronate or PBS. The graph showing the quantitative analysis of the percentage of F4/80⁺/MHCII⁺ macrophages in the spleen. n = 3 mice. **b-e**, To explore the role of macrophage EVs release in host EVs level regulation during infection, macrophage-depleted mice were injected intravenously with an equal volume of PBS, BMDM, or Rab27a shRNA-transfected BMDM for 36 hours, followed by S.Tm infection. **b**, The concentration of EVs in serum at 12 hours after S.Tm infection. n = 5 mice. **c**, The iron level in serum at 12 hours after S.Tm infection. n = 5 mice.

d, Viable count of S.Tm in the blood at 12 hours after S.Tm infection. n = 5 mice. **e**, Survival rates of mice. n = 6 mice. **f**, To determine whether macrophage is the major source of serum EVs induced by HKS.Tm, macrophage-depleted mice were treated with an equal volume of PBS or BMDM for 36 hours, followed by HKS. Tm treatment. The graph showed the concentration of EVs in serum. n = 5 mice. For **a-d** and **f**, data are presented as the mean ± s.d. For **a**, statistical significance was assessed by unpaired two-tailed Student's t-test. For **b-d** and **f**, statistical significance was assessed by one-way ANOVA with Tukey's post-hoc test. For **e**, statistical significance was performed using the log-rank test.
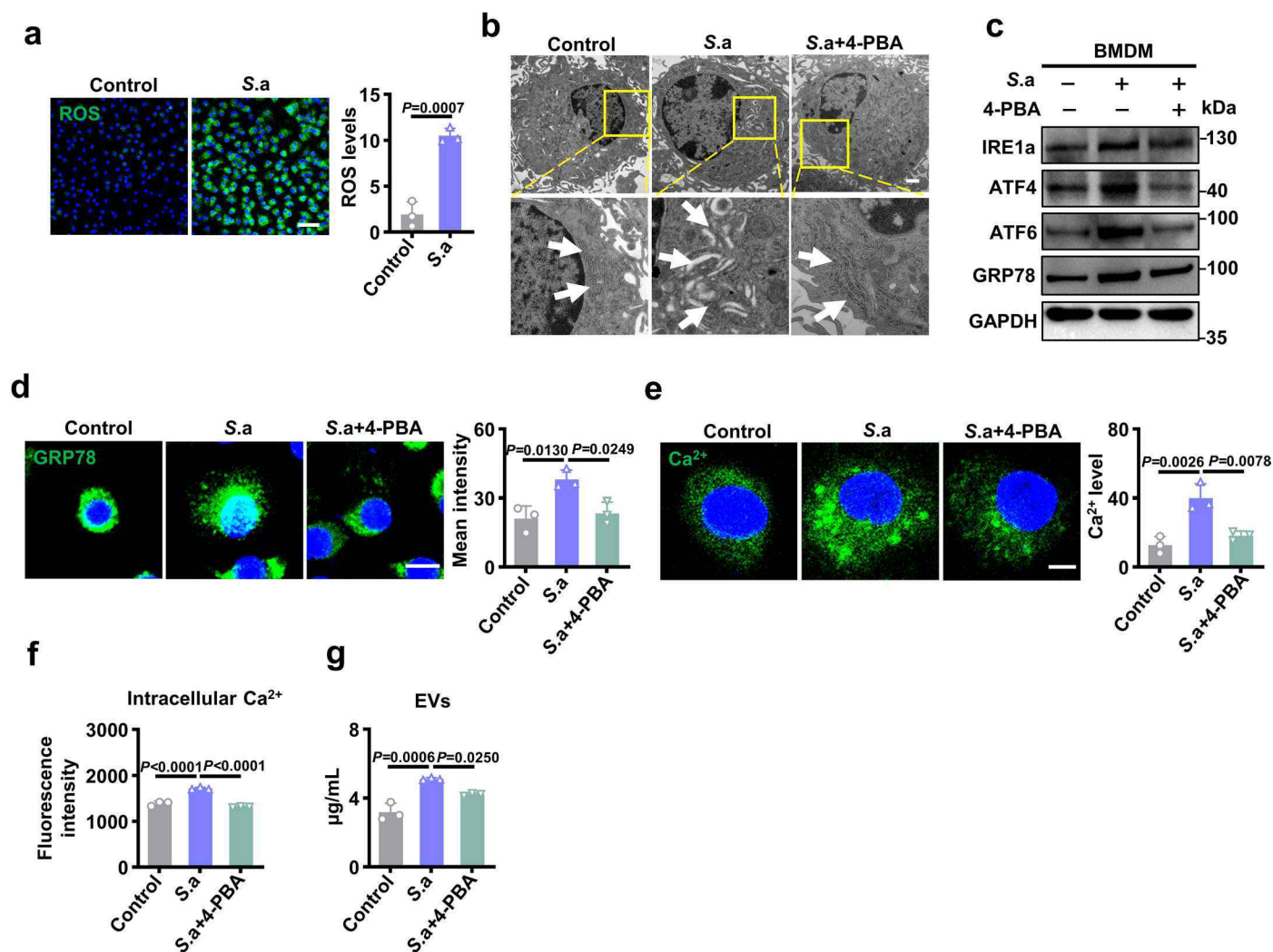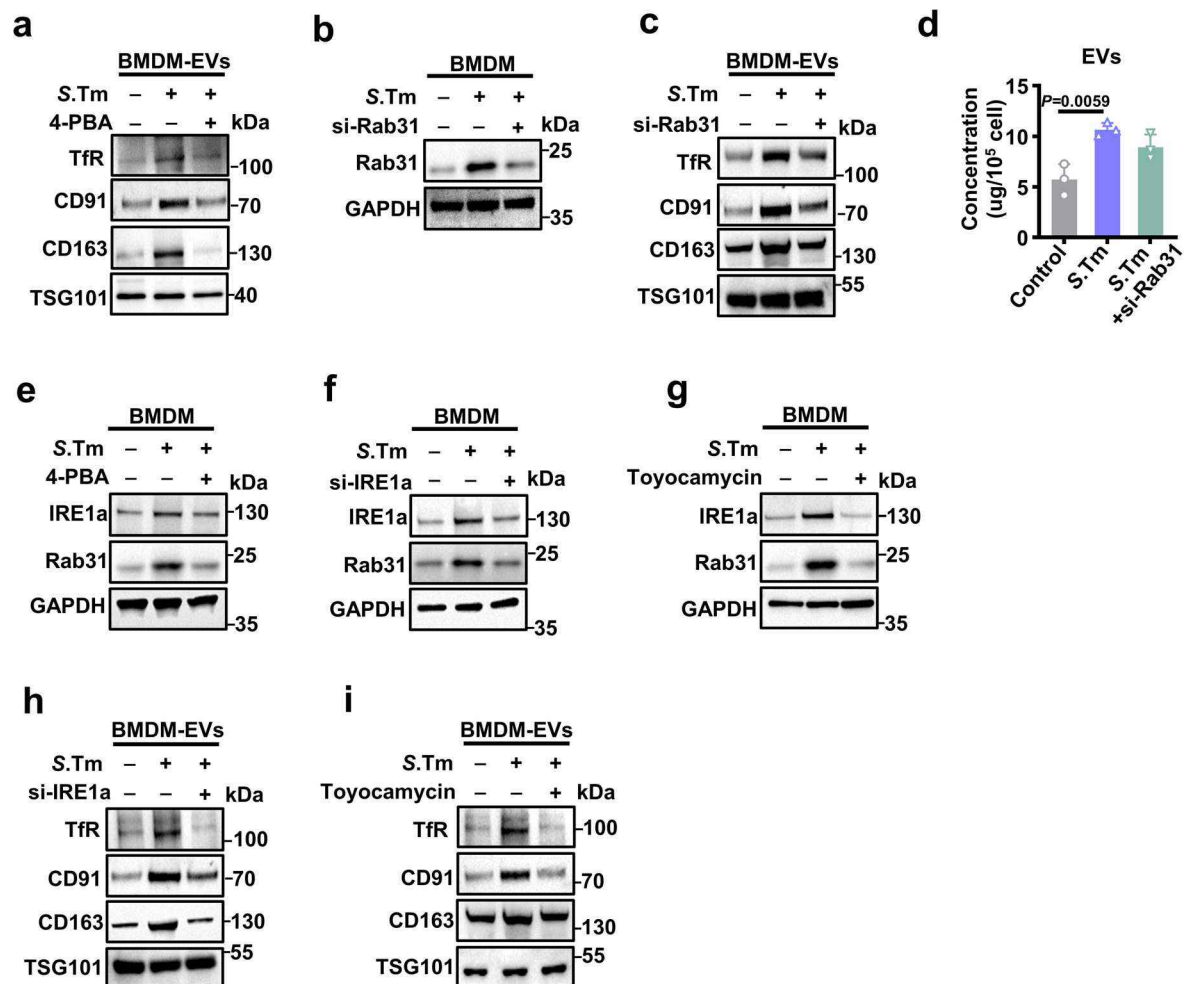
Extended Data Fig. 8 | S.a infection induces EVs release via endoplasmic reticulum stress. a, Representative fluorescence images of ROS in BMDM infected with S.a at a MOI of 25, and quantitative analysis of the ROS levels in cells. Scale bar, 50 μm. n = 3 biologically independent samples. **(b-g)**, BMDM were infected with S.a in the absence or presence of 4-PBA to clarify the association between ERS and EVs release. **b**, TEM images showed the ultrastructural morphology of the endoplasmic reticulum in BMDM. Scale bar, 1 μm. High-magnification images of the area marked by yellow boxes are arrayed at the lower panel. White arrow indicated endoplasmic reticulum. **c**, Western blot analysis of the expression of IRE1α, ATF4, ATF6 and GRP78 in BMDM. In **b** and **c**, experiments were repeated three times and representative images are shown.

d, Representative fluorescence images of GRP78 in BMDM, and quantitative analysis of the fluorescence intensity Scale bar, 10 μm. n = 3 biologically independent samples. **e**, Representative fluorescence images of intracellular Ca²⁺ level in cells, and quantitative analysis of the Ca²⁺ levels. Scale bar, 4 μm. n = 3 biologically independent samples. **f**, Intracellular Ca²⁺ levels measured by fluorescence intensity. n = 3 biologically independent samples. **g**, The concentration of EVs in supernatant. n = 3 biologically independent samples. For **a** and **d-g**, data are presented as the means ± s.d. For **a**, statistical significance was analyzed by unpaired two-tailed Student's t-test. For **d-g**, statistical significance was analyzed by one-way ANOVA with Tukey's post-hoc test.
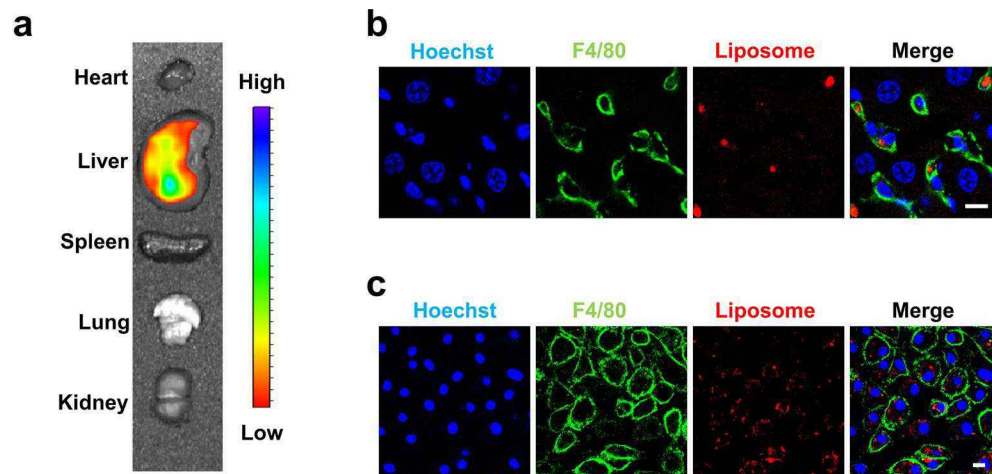
Extended Data Fig. 9 | The biodistribution of 4-PBA-encapsulated liposome.
a, *Ex vivo* fluorescent images of various organs in mice injected with RhB-labeled 4-PBA-encapsulated liposome. n = 3 mice. **b,c**, The uptake of RhB-labeled liposome (red) by macrophages in liver **(b)** or *in vitro* cultured BMDM **(c)** stained with Hoechst (nucleus; blue) and F4/80 (cell membrane; green). Scale bar, 10 μm. n = 3 biologically independent sample.

a BMDM-EVs

S.Tm − + +
4-PBA − − + kDa

TfR — 100
CD91 — 70
CD163 — 130
TSG101 — 40

b BMDM

S.Tm − + +
si-Rab31 − − + kDa

Rab31 — 25
GAPDH — 35

c BMDM-EVs

S.Tm − + +
si-Rab31 − − + kDa

TfR — 100
CD91 — 70
CD163 — 130
TSG101 — 55

d EVs

e BMDM

S.Tm − + +
4-PBA − − + kDa

IRE1a — 130
Rab31 — 25
GAPDH — 35

f BMDM

S.Tm − + +
si-IRE1a − − + kDa

IRE1a — 130
Rab31 — 25
GAPDH — 35

g BMDM

S.Tm − + +
Toyocamycin − − + kDa

IRE1a — 130
Rab31 — 25
GAPDH — 35

h BMDM-EVs

S.Tm − + +
si-IRE1a − − + kDa

TfR — 100
CD91 — 70
CD163 — 130
TSG101 — 55

i BMDM-EVs

S.Tm − + +
Toyocamycin − − + kDa

TfR — 100
CD91 — 70
CD163 — 130
TSG101 — 55

Extended Data Fig. 10 | Rab31 regulates the enrichment of iron-related receptors onto EVs. a, BMDM were treated with *S*.Tm in the absence or presence of 4-PBA for 24 hours, then EVs were isolated. The TfR, CD91, CD163, and TSG101 expressions on EVs were detected by Western blot. **b-d**, BMDM were pretreated with Rab31-siRNA and then infected with *S*.Tm. EVs from BMDM were isolated at 24 hours after *S*.Tm infection. The Rab31 expressions in BMDM **(b)** and TfR, CD91, CD163, and TSG101 expressions on EVs **(c)** were detected by Western blot. **d**, The concentration of EVs released by BMDM. n = 3 biologically independent samples. **e**, BMDM were treated with *S*.Tm in the absence or presence of 4-PBA for 24 hours.

The IRE1α and Rab31 expressions in BMDM were detected by Western blot. **f-i**, BMDM were pretreated with IRE1α-siRNA **(f,h)** or toyocamycin **(g,i)** respectively and then were infected with *S*.Tm. The IRE1α and Rab31 expressions in BMDM **(f, g)**, and TfR, CD91, CD163, and TSG101 expressions on EVs from BMDM **(h,i)** were analyzed by Western blot. For **d**, data are presented as the means ± s.d. For **d**, statistical significance was analyzed by one-way ANOVA with Tukey's post-hoc test. All western blots were repeated three times and representative images are shown.

nature portfolio

Corresponding author(s): Shiyu Liu, Yan Jin

Last updated by author(s): Nov 27, 2022

Reporting Summary

Nature Portfolio wishes to improve the reproducibility of the work that we publish. This form provides structure for consistency and transparency in reporting. For further information on Nature Portfolio policies, see our Editorial Policies and the Editorial Policy Checklist.

Statistics

For all statistical analyses, confirm that the following items are present in the figure legend, table legend, main text, or Methods section.

n/a	Confirmed	
☐	☒	The exact sample size (*n*) for each experimental group/condition, given as a discrete number and unit of measurement
☐	☒	A statement on whether measurements were taken from distinct samples or whether the same sample was measured repeatedly
☐	☒	The statistical test(s) used AND whether they are one- or two-sided *Only common tests should be described solely by name; describe more complex techniques in the Methods section.*
☒	☐	A description of all covariates tested
☐	☒	A description of any assumptions or corrections, such as tests of normality and adjustment for multiple comparisons
☐	☒	A full description of the statistical parameters including central tendency (e.g. means) or other basic estimates (e.g. regression coefficient) AND variation (e.g. standard deviation) or associated estimates of uncertainty (e.g. confidence intervals)
☐	☒	For null hypothesis testing, the test statistic (e.g. F, t, r) with confidence intervals, effect sizes, degrees of freedom and P value noted *Give P values as exact values whenever suitable.*
☒	☐	For Bayesian analysis, information on the choice of priors and Markov chain Monte Carlo settings
☒	☐	For hierarchical and complex designs, identification of the appropriate level for tests and full reporting of outcomes
☒	☐	Estimates of effect sizes (e.g. Cohen's *d*, Pearson's *r*), indicating how they were calculated

Our web collection on statistics for biologists contains articles on many of the points above.

Software and code

Policy information about availability of computer code

Data collection	NTA data were collected from Zeta View software v8.04.02. Western blot images were obtained on Tanon. CLSM images were obtained on NIS-Element Viewer v4.5. TEM images were obtained on TEM (TECNAI Spirit, FEI). The flow cytometry data were collected on Beckman Coulter Cytoflex. The concentration of EVs was measured by Nanosight NS300.
Data analysis	GraphPad Prism v8.0, ImageJ v1.8, IVIS Living imaging v4.3, Flowjo v10.8.1 and SPSS Statistics v19.0 were used for data analysis.

For manuscripts utilizing custom algorithms or software that are central to the research but not yet described in published literature, software must be made available to editors and reviewers. We strongly encourage code deposition in a community repository (e.g. GitHub). See the Nature Portfolio guidelines for submitting code & software for further information.

Data

Policy information about availability of data

All manuscripts must include a data availability statement. This statement should provide the following information, where applicable:
- Accession codes, unique identifiers, or web links for publicly available datasets
- A description of any restrictions on data availability
- For clinical datasets or third party data, please ensure that the statement adheres to our policy

All the data supporting the findings of this study are available within this article and the Supplementary Information files. Source data for all figures are provided. Other information of this study is available from the corresponding author upon reasonable request.

Field-specific reporting

Please select the one below that is the best fit for your research. If you are not sure, read the appropriate sections before making your selection.

[✗] Life sciences   [ ] Behavioural & social sciences   [ ] Ecological, evolutionary & environmental sciences

For a reference copy of the document with all sections, see nature.com/documents/nr-reporting-summary-flat.pdf

Life sciences study design

All studies must disclose on these points even when the disclosure is negative.

Sample size	No statistical method was used to predetermined the sample size. For the in vitro experiments, at least 3 biologically independent samples were used. For in vivo experiments, 3 to 6 mice per group were used. Sample sizes were determined according to previous experimental experience and publications (PMIDs: 24658075, 15531878, 33159193, 32832662), and were sufficient for statistical analysis.
Data exclusions	No data were excluded.
Replication	The experiments were repeated at least twice, and could be reliably reproduced.
Randomization	Samples and animals were chosen at random for each experimental group. For cell experiments, cells from same source were allowed to different plates and then treated with corresponding conditions. For animal experiments, the age-matched mice were randomly assigned to treatment groups.
Blinding	Histological assessment and scoring were performed in a blinded manner. For other experiments, investigators were not blinded since they needed to perform theses experiments with different treatments.

Reporting for specific materials, systems and methods

We require information from authors about some types of materials, experimental systems and methods used in many studies. Here, indicate whether each material, system or method listed is relevant to your study. If you are not sure if a list item applies to your research, read the appropriate section before selecting a response.

Materials & experimental systems

n/a	Involved in the study
[ ]	[✗] Antibodies
[✗]	[ ] Eukaryotic cell lines
[✗]	[ ] Palaeontology and archaeology
[ ]	[✗] Animals and other organisms
[✗]	[ ] Human research participants
[✗]	[ ] Clinical data
[✗]	[ ] Dual use research of concern

Methods

n/a	Involved in the study
[✗]	[ ] ChIP-seq
[ ]	[✗] Flow cytometry
[✗]	[ ] MRI-based neuroimaging

Antibodies

Antibodies used	anti-CD81 antibody (Rabbit monoclonal EPR4244, Abcam, ab109201, lot. no.GR3360240-3, dilution: 1:1000 for WB); anti-TSG101 antibody (Rabbit monoclonal EPR7130(B), Abcam, ab125011, lot. no.GR3405595-1, dilution: 1:1000 for WB); anti-Calnexin antibody (Rabbit polyclonal, Abcam, ab22595, lot. no. GR3359380-2, dilution: 1:1000 for WB); anti-Transferrin Receptor antibody (Rabbit polyclonal, Abcam, ab84036, lot. no.GR3369964-1, dilution: 1:1000 for WB, 1:20 for immunogold staining); anti-CD91 antibody (Rabbit monoclonal EPR3724, Abcam, ab92544, lot. no. GR259330-42, dilution: 1:1000 for WB, 1:20 for immunogold staining); anti-CD163 antibody (Rabbit monoclonal EPR19518, Abcam, ab182422, lot. no. GR3339055-7, dilution: 1:1000 for WB, 1:20 for immunogold staining); anti-ATF6 antibody (Rabbit polyclonal, Abcam, ab203119, lot. no. GR3284728-3, dilution: 1:1000 for WB); anti-ATP6V1A antibody (Rabbit monoclonal EPR19270, Abcam, ab199326, lot. no. GR3210145-8, dilution: 1:1000 for WB); anti-ATP6V1B antibody (Rabbit monoclonal EPR16401, Abcam, ab200839, lot. no. GR305548-7, dilution: 1:1000 for WB); anti-GRP78 antibody (Rabbit polyclonal, Abcam, ab21685, lot. no. GR3281961-1, dilution: 1:1000 for WB, 1:200 for IF); anti-LAMP1 antibody (Rabbit polyclonal, Abcam, ab24170, dilution: 1:1000 for WB, 1:200 for IF); anti-Rab31 antibody (Rabbit polyclonal, Abcam, ab230881, lot.no. GR3417018-5, dilution1:1000 for WB); anti-Salmonella typhimurium LPS antibody (Mouse monoclonal 1E6, Abcam, ab8274, lot.no. GR3398476-1, dilution: 1:200 for IF); anti-FPN1 antibody (Rabbit polyclonal, Invitrogen, PA5-115915, dilution 1:1000 for WB); anti-CD63 antibody (mouse monoclonal MX-49.129.5, Santa Cruz Biotechnology, cat. no. sc-5275, lot. no. H2418, dilution: 1:1000 for WB); anti-FTH1 antibody (Cat#3998S, Cell Signaling Technology, Lot.no.2, dilution: 1:1000 for WB); anti-Alix antibody (Cat#92880, Cell Signaling Technology, Lot.no.1, dilution: 1:1000 for WB); anti-ATF4 antibody (Cat#11815, Cell Signaling Technology, Lot.no.2, dilution: 1:1000 for WB); anti-IRE1α antibody (Cat#3294P, Cell Signaling Technology, Lot.no.12, dilution: 1:1000 for WB); anti-TFEB antibody (Cat#32361S, Cell Signaling Technology, Lot.no.2, dilution: 1:1000 for WB); anti-Erk1/2 antibody (Cat#9102s, Cell Signaling Technology, Lot.no.27, dilution: 1:1000 for WB); anti-Phospho-Erk1/2 antibody (Cat#9101s, Cell Signaling Technology, Lot.no.30, dilution: 1:1000 for WB); anti-F4/80 antibody (Rat monoclonal Cl:A3-1, Abcam, ab6640, lot. no. GR3250648-1, dilution: 1:200 for IF);

anti-Macrophage antibody (Mouse monoclonal MAC387, Abcam, ab22506, lot. no. 864160, dilution: 1:200 for IF); anti-GAPDH antibody (YESEN, Cat.30201ES60, Lot.no.G3112040, dilution: 1:1000 for WB); peroxidase AffiniPure goat anti-mouse IgG (DIYIBio, Cat.no. DY60203); peroxidase AffiniPure goat anti-rabbit IgG (DIYIBio, Cat.no. DY60202); Alexa Fluor 488 AffiniPure goat anti-mouse (YESEN, Cat.33206ES60, lot. no. A0010031, dilution: 1:200 for IF); Alexa Fluor 594 AffiniPure goat anti-mouse (YESEN, Cat.no. 33212ES60, lot. no. A9927610, dilution: 1:200 for IF); Alexa Fluor 488 AffiniPure goat anti-rabbit (YESEN, Cat.no. 33107ES60, lot.no. F1104020, dilution: 1:200 for IF); Alexa Fluor 594 AffiniPure goat anti-rabbit (YESEN, Cat.no.33108ES60, lot. no. C2926471, dilution: 1:200 for IF); PE-conjugated anti-mouse F4/80 antibody (Cat#123110, Biolegend, Lot.no. B309222, dilution:1:100 for FC); FITC-conjugated anti-mouse CD11b antibody (Cat#101206, Biolegend, Lot.no.B358165, dilution:1:100 for FC); PE-conjugated anti-mouse MHCⅡ antibody (#116407, Biolegend, dilution:1:100 for FC); Alexa Fluor 488 anti-mouse F4/80 antibody (Cat#123120, Biolegend, Lot.no.B272102, dilution:1:100 for FC).

Validation	All antibodies are purchased from commercial resources. Validation statements can be found on the manufacturer's website for the following: anti-CD81 antibody (Abcam, ab109201): https://www.abcam.cn/cd81-antibody-epr4244-ab109201.html anti-TSG101 antibody (Abcam, ab125011): https://www.abcam.cn/tsg101-antibody-epr7130b-ab125011.html anti-Calnexin antibody (Abcam, ab22595): https://www.abcam.cn/calnexin-antibody-er-marker-ab22595.html anti-Transferrin Receptor antibody (Abcam, ab84036): https://www.abcam.cn/transferrin-receptor-antibody-ab84036.html anti-CD91 antibody (Abcam, ab92544): https://www.abcam.cn/lrp1-antibody-epr3724-ab92544.html anti-CD163 antibody (Abcam, ab182422): https://www.abcam.cn/cd163-antibody-epr19518-ab182422.html anti-ATF6 antibody (Abcam,ab203119): https://www.abcam.cn/atf6-antibody-ab203119.html anti-ATP6V1A antibody (Abcam, ab199326): https://www.abcam.cn/atp6v1a-antibody-epr19270-ab199326.html anti-ATP6V1B antibody (Abcam, ab200839): https://www.abcam.cn/atp6v1b1--atp6v1b2-antibody-epr16401-ab200839.html anti-GRP78 antibody (Abcam, ab21685): https://www.abcam.cn/grp78-bip-antibody-ab21685.html anti-LAMP1 antibody (Abcam, ab24170): https://www.abcam.cn/lamp1-antibody-lysosome-marker-ab24170.html anti-Rab31 antibody (Abcam, ab230881): https://www.abcam.cn/rab31-antibody-ab230881.html anti-Salmonella typhimurium LPS antibody (Abcam, ab8274): https://www.abcam.cn/salmonella-typhimurium-lps-antibody-1e6-ab8274.html anti-FPN1 antibody (Invitrogen, PA5-115915): https://www.thermofisher.cn/cn/zh/antibody/product/Ferroportin-Antibody-Polyclonal/PA5-115915 anti-CD63 antibody (Santa Cruz Biotechnology, cat. no. sc-5275): https://www.scbt.com/p/cd63-antibody-mx-49-129-5?requestFrom=search anti-FTH1 antibody (Cell Signaling Technology,Cat#3998S): https://www.cellsignal.com/products/primary-antibodies/fth1-antibody/3998?site-search-type=Products&N=4294956287&Ntt=fth1&fromPage=plp anti-Alix antibody (Cat#92880, Cell Signaling Technology): https://www.cellsignal.com/products/primary-antibodies/alix-e6p9b-rabbit-mab/92880?site-search-type=Products&N=4294956287&Ntt=+anti-alix+antibody&fromPage=plp anti-ATF4 antibody (Cat#11815, Cell Signaling Technology): https://www.cellsignal.com/products/primary-antibodies/atf-4-d4b8-rabbit-mab/11815?site-search-type=Products&N=4294956287&Ntt=anti-atf4+antibody+&fromPage=plp anti-IRE1α antibody (Cat#3294, Cell Signaling Technology): https://www.cellsignal.com/products/primary-antibodies/ire1a-14c10-rabbit-mab/3294?site-search-type=Products&N=4294956287&Ntt=ire1%CE%B1+antibody&fromPage=plp anti-TFEB antibody (Cat#32361S, Cell Signaling Technology): https://www.cellsignal.com/products/primary-antibodies/tfeb-d4l2p-rabbit-mab/32361?site-search-type=Products&N=4294956287&Ntt=tfeb&fromPage=plp anti-Erk1/2 antibody (Cat#9102s, Cell Signaling Technology): https://www.cellsignal.com/products/primary-antibodies/p44-42-mapk-erk1-2-antibody/9102?site-search-type=Products&N=4294956287&Ntt=anti-erk1%2F2&fromPage=plp anti-Phospho-Erk1/2 antibody (Cat#9101s, Cell Signaling Technology): https://www.cellsignal.com/products/primary-antibodies/p44-42-mapk-erk1-2-antibody/9102?site-search-type=Products&N=4294956287&Ntt=anti-erk1%2F2&fromPage=plp anti-F4/80 antibody (Abcam, ab6640): https://www.abcam.cn/f480-antibody-cia3-1-macrophage-marker-ab6640.html anti-Macrophage antibody (Abcam, ab22506): RRID:AB_447111 anti-GAPDH antibody (YESEN, Cat.no.30201ES60): https://www.yeasen.com/products/detail/881 Alexa Fluor 488 AffiniPure goat anti-mouse (YESEN, Cat.no.33206ES60): https://www.yeasen.com/products/detail/427 Alexa Fluor 594 AffiniPure goat anti-mouse (YESEN, Cat.no.33212ES60): https://www.yeasen.com/products/detail/462 Alexa Fluor 488 AffiniPure goat anti-rabbit (YESEN, Cat.no.33107ES60): https://www.yeasen.com/products/detail/347 Alexa Fluor 594 AffiniPure goat anti-rabbit (YESEN, Cat.no.33108ES60): https://www.yeasen.com/products/detail/352 PE-conjugated anti-mouse F4/80 antibody (Cat#123110, Biolgend): https://www.biolegend.com/en-us/products/pe-anti-mouse-f4-80-antibody-4068 FITC-conjugated anti-mouse CD11b antibody (Cat#101206, Biolgend): https://www.biolegend.com/en-us/products/fitc-anti-mouse-human-cd11b-antibody-347 PE-conjugated anti-mouse MHCⅡ antibody (Cat#116407, Biolgend): https://www.biolegend.com/en-us/products/pe-anti-mouse-i-ab-antibody-1741 Alexa Fluor 488 anti-mouse F4/80 antibody (Cat#123120, Biolgend): https://www.biolegend.com/en-us/products/alexa-fluor-488-anti-mouse-f4-80-antibody-4073

Animals and other organisms

Policy information about studies involving animals; ARRIVE guidelines recommended for reporting animal research

Laboratory animals	Wide-type 6-8 week-old female C57BL/6J mice were obtained from the Laboratory Animal Research Center of the Fourth Military Medical University, Xi'an, China. All mice were housed in 12 hour dark/12 hour light phases with 22 ± 2 °C and 40% humidity.
Wild animals	No wild animals were involved in the study.
Field-collected samples	No field-collected samples were used in this study.

| Ethics oversight | All animals experiments were performed in accordance with the guidelines of Intramural Animal Use and Care Committee of the Fourth Military Medical University. |

Note that full information on the approval of the study protocol must also be provided in the manuscript.

Flow Cytometry

Plots

Confirm that:

- [x] The axis labels state the marker and fluorochrome used (e.g. CD4-FITC).
- [x] The axis scales are clearly visible. Include numbers along axes only for bottom left plot of group (a 'group' is an analysis of identical markers).
- [x] All plots are contour plots with outliers or pseudocolor plots.
- [x] A numerical value for number of cells or percentage (with statistics) is provided.

Methodology

Sample preparation	BMDM were incubated with PE-conjugated anti-mouse F4/80 antibody and FITC-conjugated anti-mouse CD11b antibody at 4 °C for 1 hour. Mouse spleen was homogenized, filtered through cell strainer, and subjected to red cell lysis buffer. The cell suspension was then incubated with PE-conjugated anti-mouse MHC Ⅱ antibody and Alexa Fluor 488 anti-mouse F4/80 antibody at 4 °C for 1 hour. After incubation, these samples were analyzed via flow cytometry.
Instrument	FACS was performed using CytoFLEX flow cytometer (Bechman Coulter, USA).
Software	Data were analyzed using FlowJo software (Flow Jo LLC, USA).
Cell population abundance	For each sample, at least 20000 cells were collected.
Gating strategy	Initial cell populations were gated using an FSC and SSC plot. The gate was set to remove cell debris (small FSC v SSC) and large clumps or aggregates of cells (large FSC or SSC), and used across all samples. BMDM were then gated as CD11b+ or F4/80+. Splenic macrophages were gated as F4/80+MHC Ⅱ+.

- [x] Tick this box to confirm that a figure exemplifying the gating strategy is provided in the Supplementary Information.